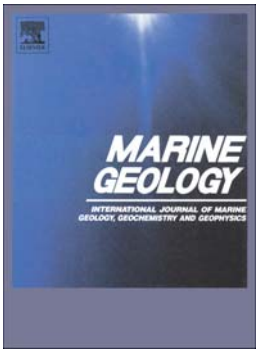

Records of continental slope sediment flow morphodynamic responses to gradient and active faulting from integrated AUV and ROV data, offshore Palos Verdes, southern California borderland

Katherine L. Maier, Daniel S. Brothers, Charles K. Paull, Mary McGann, David W. Caress, James E. Conrad

PII: S0025-3227(16)30230-4
DOI: doi: 10.1016/j.margeo.2016.10.001
Reference: MARGO 5519

To appear in: *Marine Geology*

Received date: 14 March 2016
Revised date: 15 September 2016
Accepted date: 2 October 2016

Please cite this article as: Maier, Katherine L., Brothers, Daniel S., Paull, Charles K., McGann, Mary, Caress, David W., Conrad, James E., Records of continental slope sediment flow morphodynamic responses to gradient and active faulting from integrated AUV and ROV data, offshore Palos Verdes, southern California borderland, *Marine Geology* (2016), doi: 10.1016/j.margeo.2016.10.001

Records of continental slope sediment flow morphodynamic responses to gradient and active faulting from integrated AUV and ROV data, offshore Palos Verdes, southern California Borderland

Katherine L. Maier[1*], Daniel S. Brothers[1], Charles K. Paull[2], Mary McGann[3], David W. Caress[2], and James E. Conrad[1]

[1]*U.S. Geological Survey, Pacific Coastal and Marine Science Center, 2885 Mission Street, Santa Cruz, CA 95060*

[2]*Monterey Bay Aquarium Research Institute, 7700 Sandholdt Road, Moss Landing, CA 95039*

[3]*U.S. Geological Survey, Pacific Coastal and Marine Science Center, 345 Middlefield Road, Menlo Park, CA 94025*

**corresponding author: kcoble@usgs.gov*

ABSTRACT

Variations in seabed gradient are widely acknowledged to influence deep-water deposition, but are often difficult to measure in sufficient detail from both modern and ancient examples. On the continental slope offshore Los Angeles, California, autonomous underwater vehicle, remotely operated vehicle, and shipboard methods were used to collect a dense grid of high-resolution multibeam bathymetry, chirp sub-bottom profiles, and targeted sediment core samples that demonstrate the influence of seafloor gradient on sediment accumulation, depositional environment, grain size of deposits, and seafloor morphology. In this setting, restraining and releasing bends along the active right-lateral Palos Verdes Fault create and maintain variations in seafloor gradient. Holocene down-slope flows appear to have been generated by slope failure, primarily on the uppermost slope (~100–200 m water depth). Turbidity currents created a low relief (<10 m) channel, up-slope migrating sediment waves (λ = ~100 m, h=<2 m), and a series of depocenters that have accumulated up to 4 m of Holocene sediment. Sediment waves increase in wavelength and decrease in wave height with decreasing gradient. Integrated analysis of high-resolution datasets provides quantification of morphodynamic sensitivity to seafloor gradients acting throughout deep-water depositional systems. These results help to bridge gaps in scale between existing deep-sea and experimental datasets and may provide constraints for future numerical modeling studies.

Keywords: gradient; deep-water channel; sediment waves; Holocene; turbidite; fault

1. Introduction

Deep-sea deposits can record local to global scale processes and are frequently used to interpret changes through time in sediment transport, climate, ecosystems, and marine geohazards (e.g., Prins et al., 2000; Normark et al., 2009a; Nunoura et al., 2009; Wang et al., 2015). Continental slope settings are important areas of transition in offshore sediment transport, including complex juxtaposition between sediment accumulation, bypass, and erosion (e.g., Rona, 1969; Lewis and Kohn, 1973; Shepard, 1981; Klaucke et al., 2000; Hodgson and Flint, 2005; Mitchell and Huthnance, 2008; McHargue et al., 2011). In order to accurately interpret depositional records from the continental slope and other deep-water settings, a detailed understanding of fine-scale sediment flow dynamics and relation to seafloor morphology is needed.

Many deep-sea depositional features, such as sediment waves (e.g., Migeon et al., 2000; Wynn et al., 2000a,b; Ercilla et al., 2002a,b; Normark et al., 2002), channel-lobe transition zones (e.g., Normark and Piper, 1983; Mutti and Normark, 1987; Wynn et al., 2002), and shifts in channel confinement and architecture (Kneller, 2003; Adeogba et al., 2005; Maier et al., 2011, 2013; Paull et al., 2011 and many others), can be related to variations in gradient, which is a fundamental parameter governing flows. Deposition and sediment accumulation are thought to preferentially occur in low gradient segments or areas below an equilibrium profile; conversely, areas of steeper gradient or above equilibrium profile preferentially experience erosion or bypass (e.g., Ross et al., 1994; Pirmez et al., 2000; Kneller, 2003; Samuel et al., 2003; Ferry et al., 2005; Brothers et al., 2013; Georgiopoulou and Cartwright, 2013; Micallef et al., 2014) (Fig. 1). Breaks in gradient are recognized to induce hydraulic jumps in sediment gravity flows, triggering erosion followed by enhanced deposition on the lower gradient segments (Komar, 1971; Mutti and Normark,

1987; García, 1993). Hydraulic jumps are increasingly recognized as an important part of depositional and erosional processes on the continental margin (e.g., Piper et al., 1999; Fildani et al., 2006, 2013; Piper and Normark, 2009), and advances over the past decade facilitate observation and quantification of seafloor gradient and morphologies at scales approaching outcrop observations (e.g., Caress et al., 2008; Paull et al., 2011, 2013; Maier et al., 2013). Although modeling requires additional inputs such as velocity and entrainment, this study provides fine-scale measurements of grain size, morphology, gradient, and estimates of flow height and concentration like those needed in recent numerical modeling studies (e.g., Cartigny et al., 2011; Kostic, 2014; Traer et al., 2015)

Deep-sea environments on the modern seafloor provide opportunities to study in detail seafloor morphology resulting from recent sediment gravity flow deposits, using high-resolution bathymetry, subsurface profiling, and sediment core samples (e.g., Paull et al., 2010, 2011, 2013, 2014; Maier et al., 2011, 2012, 2013; Covault et al., 2014; Brothers et al., 2015). A recent marine paleoseismic study examining a high-resolution seafloor and shallow subsurface dataset in the southern California Borderland revealed a link between seabed gradient and Holocene sediment accumulation along a section of the continental slope adjacent to the Palos Verdes Fault (Brothers et al., 2015). In this study, we integrate the high-resolution geophysical dataset and further examination of sediment core samples to test the hypothesis that gradient exerts primary influence on sediment flow morphodynamics.

2. Regional setting

The southern California Borderland (Fig. 2) developed as the North American – Pacific plate boundary evolved from a subduction zone to a transform margin in the early and middle Tertiary period (e.g., Crouch, 1981; Vedder, 1987; Crouch and Suppe, 1993;

Bohannon and Geist, 1998). The southern California Borderland is dominated by right-lateral strike-slip faults that represent the western portion of the active San Andreas Fault System (e.g., Legg, 1991; Legg et al., 2007; Fisher et al., 2009; Ryan et al., 2009) (Fig. 2). This study is focused along the Palos Verdes Fault where it ruptures the seafloor of the continental slope, offshore Los Angeles and the Palos Verdes Peninsula (Marlow et al., 2000; Brothers et al., 2015) (Fig. 3). Within the study area, the Palos Verdes Fault is present on the seafloor as an up to ~2 m scarp with subtle restraining and releasing bends and step-overs (Brothers et al., 2015) (Fig. 4). A Pleistocene submarine landslide headwall scarp (i.e., upper headwall) was identified within the study area (Fig. 4) and used to calculate late Pleistocene and Holocene lateral slip-rate estimates of 1.6–1.9 mm/yr along the Palos Verdes Fault (Brothers et al., 2015).

Within the dynamic tectonic landscape, sediments are transported from onshore and shelfal regions to deep-water basins largely via submarine canyon, channel, and fan depositional systems (e.g., Shepard and Ensele, 1962; Normark et al., 2009a,b). Canyons that head on the outer shelf or upper slope and remain kilometers away from rivers and littoral cells are effectively shut-off from terrestrial-derived sediment that is conveyed in littoral cells to shelf-incised canyons during sea-level highstands (e.g., Covault et al., 2007; Covault and Romans, 2009; Normark et al., 2009a,b; Covault and Fildani, 2014) (Fig. 2). The San Gabriel Canyon system heads ~20 km from the shoreline at Long Beach (Fig. 2). Under sea-level highstand conditions that were established by ~7–9 ka (e.g., Flemming et al., 1998; Sommerfield et al., 2009), sediment discharge from the Los Angeles and San Gabriel rivers (on the order of 1,200,000+ tons per year; Warrick and Farnsworth, 2009) is diverted away from San Gabriel Canyon and the adjacent slope via the San Pedro littoral cell.

West of San Gabriel Canyon along the Palos Verdes Fault, high-resolution surveys of the mid-continental slope reveal complex seafloor morphology formed from late Pleistocene and Holocene deposits (Brothers et al., 2015) (Fig. 4). At the proximal end of the survey area, a low-relief (<10 m), down-slope oriented channel 1–2 km west of and roughly parallel to the main San Gabriel Canyon channel is present along an active fault strand. Crescentic to sinuous wave-like bedforms interpreted to be sediment waves are oriented parallel to sub-parallel to slope contours and are present down slope from the channel. Sediment waves fill the fault-bounded pull-apart basin and continue to the steep, arcuate upper headwall scarp.

3. Methods

Approximately 24 km^2 of the continental slope in ~200–600 m water depth offshore Palos Verdes was mapped using the Monterey Bay Aquarium Research Institute (MBARI) mapping autonomous underwater vehicle (AUV) to obtain continuous high-resolution multibeam bathymetry and a grid of chirp sub-bottom profiles. The AUV was programmed to follow missions up to 8.5 hr in duration and fly 50 m above the seafloor at a speed of 3 knots. AUV tracklines were spaced at ~150 m (Fig. 3A) for continuous bathymetric swath coverage using a Reson 7100, 200-kHz multibeam sonar (Caress et al., 2008). The AUV data were processed with MB-System open-source seafloor mapping software (Caress and Chayes, 1996; Caress et al., 2008). The AUV multibeam bathymetry were gridded at 2-meter lateral resolution and have ~0.15 m vertical resolution. The AUV bathymetry were interpreted within the context of regional multibeam bathymetry, which was collected with a Kongsberg Simrad EM300 multibeam sonar and gridded at resolutions from 50 m to 10 m (Dartnell and Gardner, 1999; Gardner and Dartnell, 2002; Dartnell et al., 2014, 2015).

The AUV collected ~190 line-km of chirp sub-bottom profiles simultaneously with the multibeam bathymetry using an Edgetech 2- to 16-kHz chirp sub-bottom profiler. The resulting sub-bottom profiles have a vertical resolution of ~0.1 m for up to ~40 m below the seafloor (Caress et al., 2008). A base Holocene horizon (~10 ka), constrained by sediment cores with radiocarbon ages and mapped by Brothers et al. (2015) throughout the AUV chirp profiles using *Kingdom* software, is interpolated across the study area to create an isopach map of sediment thickness. All sub-bottom depths and stratal thicknesses were converted from time to depth assuming 1500 m/s sound velocity.

Following geophysical data collection, two sediment-core sampling efforts were undertaken across the Palos Verdes Fault (Brothers et al., 2015). The USGS recovered gravity cores in 2009 from four sites upslope from the upper headwall. In 2010, the MBARI remotely operated vehicle (ROV) *Doc Ricketts* collected 18 vibracores in the same region. All cores were archived at the U.S. Geological Survey (USGS) core repository in Menlo Park, CA. Core data utilized in this study are available in Maier et al. (2016). Whole-core samples were scanned with a GEOTEK multisensory core logger (MSCL) to generate p-wave velocity, gamma-ray density logs, and continuous digital photographs.

Five cores (DR125 VC-89, DR135 VC-131, DR136 VC-134, and PV2-G1) were scanned with x-ray commuted tomography (CT) using a GE LightSpeed Ultra instrument at a Stanford University Petroleum Research Institute (SUPRI-A) Enhanced Oil Recovery and Unconventional Resources Laboratory. Split core tubes containing ~150 cm of core material were scanned in either 1.25 mm or 2.50 mm axial slices at 120 kV and 200 mA. Coronal slice images (i.e., similar to the split core face) were generated with RadiAnt software.

Grain size analyses were conducted at the USGS Pacific Coastal and Marine Science Center Sediment Laboratory in Santa Cruz, California. Grain size samples were processed

by soaking in a hydrogen peroxide solution to remove organics, removal of salts by centrifuge, sieving into sand-to-silt (2–0.063 mm) and clay (<0.063 mm) size fractions, and treating of the clay fraction with a 10% sodium hexametaphosphate solution to disperse negatively charged clay particles. Each sample fraction was dried, weighed, and analyzed using a Beckman Coulter LS 13 320 laser diffraction particle size analyzer measuring in quarter phi bins. Resulting data for sand and mud analyses were quantitatively combined using pcSDSZ Sediment Size Analysis Software for Windows.

Radiocarbon age was analyzed on planktic (preferred) or benthic foraminifera from fine-grained beds or organic material from 2–3 cm intervals of several cores. The resulting sample separates were analyzed by accelerator mass spectrometry (AMS) at the National Ocean Sciences AMS (NOSAMS) facility at Woods Hole Oceanographic Institution. Ages were calculated using the accepted ^{14}C half-life of 5568 years (Stuiver and Polach, 1977). Marine carbonate samples were reservoir-age corrected and calibrated using a 633-year (Ingram and Southon, 1996; Stuiver and Braziunas, 1993) and 1750-year (Mix et al., 1999) reservoir age correction for planktic and benthic samples, respectively. Raw ages for marine carbonate samples were converted to calendar years using the CALIB program (Stuiver et al., 2015).

4. Results

4.1. Seafloor morphology and gradient

The region to the west of San Gabriel Canyon includes a relatively flat outer continental shelf and a continental slope with channels, ridges, and the Palos Verdes Fault Zone (Fig. 3). The shelf edge and upper slope to ~200 m water depth contain arcuate or scallop-shaped scarps. Channels appear on the upper slope below and adjacent to the scarps.

These channels converge down-slope and generally follow the trend of the Palos Verdes Fault.

The AUV survey area (Fig. 4) can be split into seven segments based on breaks in gradient and character of bedforms (Figs. 5–6). In segment (1), the low-relief channel (<10 m height, ~200 m width) extends down slope for ~1.5 km with minimal sinuosity and a mean gradient of ~1.9°. A 1–2-m-relief Palos Verdes Fault scarp forms the western channel margin. Subtle down-slope-concave crescent-shaped bedforms (<100 m wavelength; <1 m relief) are confined to the channel floor and do not appear to extend west of the Palos Verdes Fault or east of the channel thalweg.

Segment (2) begins where seafloor gradient decreases from ~1.9° to <0.5° (Figs. 5–6). At this break in gradient, the channel loses confinement on its eastern margin. Crescent to sinuous sediment wave bedforms are present across up to ~500 m on the seafloor with wavelengths and wave heights 33 m – 159 m and 0.6 m – 3.0 m, respectively. Along the fault trace, the sediment waves have a consistently up-slope-oriented convex shape, but the same sediment waves vary as they extend on both sides of the fault. The trace of the active Palos Verdes Fault and sediment waves are visible on the seafloor in segment (2) and continue through segment (5) (e.g., Fig. 7).

Where seabed gradient increases slightly to >1°, segment (2) transitions into the open slope of segment (3) (Figs. 5–6). Average wavelength of sediment waves decreases from 83 m to 65 m, and average wave height increases from 1.7 m to 1.8 m (Fig. 7). Seabed gradient drops abruptly from ~1.2° in segment (3) to <0.5° in segment (4) at the up-slope end of a pull-apart basin, corresponding to an increase in wavelength (from 65 m to 107 m) and decrease in wave relief (from 1.8 m to 1.7 m). Seabed gradient increases to ~1° – 2° in the open slope of segment (5). The transition from segment (4) to (5) corresponds to a

decrease in average wavelength (from 107 m to 68 m) and slight decrease in average sediment wave height (1.7 m to 1.6 m). A drop in gradient (from ~1° to ~0.5°) in segment (5) occurs where a splay of the Palos Verdes Fault (Fig. 4) merges into a single fault strand that intersects the upper headwall. The decrease in average sediment wave height at a gradient increase between segments (4) and (5) may be related to two more subtle breaks in gradient (from ~1.5° to 0.9° and 0.7°, respectively) that occur in the distal end of segment (5); excluding the low sediment wave height measurements in distal segment (5) results in an average of 1.8 m and an increase in wave height between segments (4) and (5).

Sediment waves are not present on the seafloor beyond segment (5) (e.g., Fig. 7). Segment (6) is a short (~100 m), very steep (20–45°) segment crossing the upper headwall of the slump scarp (Figs. 5–6). A drop in gradient occurs immediately at the base of the upper headwall, where the seafloor is flat to back-sloped by ~0.5°.

4.2. Holocene sediment isopach

Holocene sediment thickness varies between profile segments in tandem with gradients (Figs. 5–6). In segment (1), thickness drops from ~2.5 m at the proximal end to ~1 m at the distal end. Holocene sediment thins to <20 cm onto the ridge adjacent to the channel and in the channel thalweg (Fig. 8). Holocene sediment thins to ~1 m at the break in gradient between segments (1) and (2), then abruptly increases to ~4 m at a depocenter in segment (2) (Figs. 5–6), and then decreases to ~1–1.5 m in segment (3). At the distal end of segment (3), two subtle breaks in gradient (from ~1.5° to 0.9° and 0.7°, respectively) correspond to small increases (<1 m) in Holocene sediment thickness. Thick Holocene sediment (up to ~4.2 m) occurs at a break in gradient at the segment (4) pull-apart basin. Chirp profiles crossing the pull-apart basin (Figs. 9–10) illustrate that reflections of

Pleistocene-age deposits are generally parallel to sub-parallel and continuous, and overlying reflections within the Holocene package are generally less continuous and of higher amplitude.

In segments (2) through (5), aggradational, up-slope migrating bedforms are suggested by reflection geometries throughout the Holocene sediment package, where sediment waves are present on the seafloor (Fig. 10). In cross-section, the sediment waves are fairly symmetrical, and reflections are sub-parallel, onlap the up-slope side, and pinch out or downlap on the down-slope side.

At the transition from segment (4) pull-apart basin depocenter to segment (5), Holocene sediment thickness decreases to ≤0.4 m (Figs. 5–6). In segment (5), Holocene sediment thickness spikes from ~1 m to ~2 m where gradient drops slightly from ~1.2°–0.5° and a splay of the Palos Verdes Fault (Fig. 4) merges into a single fault strand on the seafloor that intersects the upper headwall down slope. Minimal Holocene sediment (<1 m) has accumulated in segment (6) on the steep (~20°–45°) upper headwall scarp. In segment (7) base of the upper headwall depocenter, Holocene sediment immediately increases to ~4 m.

4.3. Holocene deposits

Twenty two cores ranging 37 to 174 cm in length were recovered between 330 and 510 m water depths in the segment (1) channel and segments (2), (4), and (7) depocenters. The cores contain primarily bioturbated mud, a mixture of clay, silt, and very fine to fine sand (Figs. 11–13). Muddy, silt-dominated deposits are relatively homogenous, bioturbated, and contain slight color variations (within or close to Munsell color 5Y4/3). Mud units are interbedded with thin sandy layers, muddy sand, and organic-rich layers. Contacts between

units are generally sharp, and bases of sand units may be loaded, displaying flame structures. Organic material, typically platy black flecks, is concentrated in layers, and larger (cm-scale) pieces appear to be wood.

Grain size results are grouped into two categories, interpreted as flow deposits and hemipelagic background sedimentation, based on the sand content and shape of the grain size distribution curve (Table 1). Samples with D_{90} <90 microns, <25% sand, and a single skewed grain size peak at ~20–30 microns are inferred to be hemipelagic deposits. Flow deposits are distinguished by higher sand or clay content, a saddle-shaped dual grain size distribution curve, and contacts imaged in CT (Figs. 12–13). Many depositional units appear to fine upward, with decreasing sand content up-section and muddier deposits overlying sandier basal beds, interpreted to be T_a division and T_b, T_d, T_{ef} divisions of turbidites that were deposited from low-density turbidity currents (Bouma, 1962; Lowe, 1982) (e.g., Fig. 15–16).

Radiocarbon (calendar) ages range from modern to ~46 ka. All but three radiocarbon samples were mixed planktic or benthic foraminifera, and no shelfal species were encountered. Most ages are in agreement with stratigraphic superposition. Older ages out of stratigraphic order in core PV2-G1 coincide with other evidence of flow deposits from grain size analyses and CT scans (Fig. 13). Radiocarbon ages constrain four chronostratigraphic Holocene units (a, b, c, and d) defined by the base of flow deposits and compared along core transects (Figs. 11–13).

Sand content, grain size distributions, and deposit thickness vary in chronostratigraphically correlative units. An ROV vibracore transect at ~365 m water depth (e.g., Fig. 8) across the segment (1) channel to the transpressional ridge reveals variation in the apparent number, character, and depth of flow deposits across the channel in thalweg,

channel, margin, and overbank depositional environments (Fig. 11). Cores acquired across the low-relief channel are closely spaced (<220 m transect) (Fig. 8), yet deposits vary (Figs. 11–12). The thickest flow deposit (~18 cm) with the coarsest sandy layer (~7 cm with >75% sand) is present in the channel thalweg (core DR125 VC-89), and it contains concentrated, visible organic material, including a piece of wood. At the adjacent channel margin only 32 m from thalweg core DR125 VC-89, the correlative mid-Holocene organic-rich deposit (in unit c) is thinner overall (~16 cm max) and muddier (~3 cm with >50% sand).

One sediment core from mid-depocenter in segment (2) (PV9-G1) recovered minimal sediment but contains three sandy flow deposits in the upper 37 cm of sediment below the seafloor (Fig. 13). The loaded base of a sandy turbidite bed indicates rapid deposition.

Holocene deposit thickness and apparent number of Holocene event deposits increases in the segment (4) pull-apart basin depocenter (Fig. 13), where structural accommodation is created between two strands of the Palos Verdes Fault (Fig. 9). Several reflections are resolved in the Holocene section, and 15+ flow deposits are present in core DR136 VC-134, which does not sample the entire Holocene section. Flow deposits within this core are thin and muddy with individual beds typically less than 5 cm thick. Only one analyzed flow deposit had more than 50% sand.

In the segment (7) base of upper headwall depocenter, Holocene sediments are ~4 m thick to the distal extent of the study area (Fig. 5). PV2-G1 deposits lack sandy turbidites (Fig. 13). Muddy flow deposits are characterized by slightly more silt, clay, or visible organic material than the surrounding muddy hemipelagic deposits. Clay-rich flow deposits may have contained flocculated clays with settling velocities approaching that of silt or fine sand grains (e.g., Stow et al., 1980). Although extensive bioturbation illustrated in CT (Fig.

13) may mask additional bed contacts and flow deposits, units a and b appear progressively finer with slightly higher percentage clay compared to chronostratigraphically correlative deposits from up-slope segments (Fig. 6).

5. Discussion

5.1. Sediment gravity flows

In the Holocene, turbidity currents flowed in segments (1) through (7), which are located >25 km from potential sediment sources at the modern shoreline, rivers, and littoral cells (Fig. 2). Despite apparent shut-off of terrestrial sediment supply for most of the Holocene, sediment gravity flows continued to accumulate deposits on the Palos Verdes slope throughout the Holocene (Fig. 5). Mass wasting of fine-grained sediments at the shelf edge and uppermost slope scarps may have provided a sediment source for these flows (Fig. 5A) (e.g., Hampton, 1972; Mohrig and Marr, 2003; Piper and Normark, 2009).

The AUV study area appears to have experienced significant deposition (e.g., higher amplitude reflections in the pull-apart basin, more sediment waves, channelized flows, and meters of sediment accumulation) during sea-level highstand, despite disconnection from terrestrial sediment sources. For example, in the pull-apart basin, Holocene sediment is as thick as the underlying ~10 kyr of late Pleistocene sediments (Figs. 9, 10). This shift in activity and continued source of sediment to the continental slope is unexpected because southern California Borderland canyons with increased activity during sea-level highstand require incision into nearshore areas to keep connection to sediment sources (Covault et al., 2007; Covault and Romans, 2009; Covault and Fildani). If other continental slope settings offshore southern California receive similar Holocene flows, then there is additional potential with high-resolution methodologies applied in this study to produce Holocene slip

rates and paleoseismic evidence needed for southern California earthquake hazard assessment.

Numerous Holocene-active faults in the Borderland (e.g., Fisher et al. 2009; Ryan et al., 2012), the active Palos Verdes Fault in the study area (Brothers et al., 2015), and spikes in southern California fault activity in the mid-Holocene (Dolan et al., 2007) may have provided seismic triggers to initiate flows. Although earthquake triggered turbidity currents are frequently interpreted (e.g., Normark and Piper, 1991; Piper and Normark, 2009) and there appear to be ample seismic triggers for mass wasting in the study area (Fig. 2), further investigation is needed to make any direct link to seismic activity (e.g., Bernhardt et al., 2015). However, the influence of gradient on deposition and morphology documented in this study is not dependent on triggering mechanism or source of sediment, and these concepts are applicable across deep-water depositional and tectonic regimes.

5.2. Sediment waves

Sediment waves are a major depositional and morphologic feature in the study area (Fig. 7) and are common features on continental margins elsewhere (e.g., Normark et al., 1980; Wynn et al., 2000b; Kostic, 2014). Sediment waves in segments (2) through (5) display symmetrical to slightly asymmetrical, up-slope migrating cross-sections (Fig. 10), similar to sediment waves documented in other modern and ancient settings (e.g., Normark et al., 1980; Migeon et al., 2000; Wynn et al., 2000a,b and references therein; Ercilla et al., 2002a,b; Gong et al., 2012; Kuang et al., 2014, and many others). Despite these overall morphologic and cross-sectional similarities, sediment waves observed in high-resolution AUV data from the Palos Verdes slope are at least an order of magnitude smaller in wavelength and amplitude than sediment waves documented from other settings (e.g.,

Normark et al., 1980 and references therein; Migeon et al., 2000; Wynn et al., 2000a,b; Ercilla et al., 2002a,b; Normark et al., 2002 and references therein; Wynn and Stow, 2002 and references therein; Gong et al., 2012; Kuang et al., 2014; Perez-Hernandez et al., 2014*).* Wavelengths have been documented over 4 km (Wynn and Stow, 2002) and are frequently observed over 2 km (Migeon et al., 2000; Wynn et al., 2000b; Normark et al., 2002; Wynn and Stow, 2002; Gong et al., 2012; Kuang et al., 2014). Corresponding sediment wave heights are up to 80 m or greater (e.g., Wynn and Stow, 2002; Gong et al., 2012; Perez-Hernandez et al., 2014), and are infrequently measured at less than 10 m outside of submarine canyons (e.g., Migeon et al., 2000; Wynn et al., 2000a,b). Although the dimensions of sediment waves in this study are distinctly smaller than many other examples, they have a wavelength to wave height ratio within the range of that for sediment waves reported in the literature from slopes less than 2° (e.g., Wynn et al., 2000b; Gong et al., 2012; Perez-Hernandez et al., 2014). Similar to other documented sediment wave fields (e.g., Ercilla et al., 2002a,b), the Palos Verdes sediment waves also increase in wavelength and decrease in wave height with decreasing gradient (Fig. 7). These similarities suggest that the Palos Verdes slope sediment waves are likely bedforms formed by similar depositional processes to larger-scale sediment waves. Although Palos Verdes sediment waves are smaller than most existing examples, features of this size cannot be resolved given the data resolution of most mapping systems. Smaller-scale sediment waves and the depositional processes they represent may turn out to be more common on continental margins as additional areas are surveyed at higher resolution.

Sediment waves (net depositional cyclic steps) and other bedforms observed in this study are at least an order of magnitude smaller than erosional cyclic steps documented in submarine canyons and channels (e.g., Fildani et al., 2006; Maier et al., 2011, 2013; Covault

et al., 2014; Zhong et al., 2015), but have similar wavelength and amplitude to sand waves (Smith et al., 2005, 2007) and crescent-shaped bedforms (Normark et al., 2009c; Paull et al., 2010, 2011, 2013; Tubau et al., 2015) documented in high-resolution multibeam bathymetry from canyons that have remained active during Modern sea-level highstand conditions (e.g., Monterey Canyon (Paull et al., 2010, 2011), La Jolla Canyon (Paull et al., 2013), and Redondo Canyon (Normark et al., 2009c)). Indistinct bedforms on the low-relief channel floor (Fig. 4) may be analogous to crescent-shaped bedforms imaged in similar-scale high-resolution data from canyons offshore California. However, the Palos Verdes slope sediment waves are interpreted to represent depositional processes occurring on the unconfined slope.

Sediment waves imaged in this study are interpreted to have formed from fine-grained, unconfined, low-density, turbidity currents flowing down slope out of the low-relief channel. Seafloor data support this interpretation because the sediment wave crests are oriented approximately parallel to slope contours, the wave field is located immediately down slope from a channel (Fig. 7), and the feeder channel is oriented approximately perpendicular to slope contours (Fig. 4). Chirp profiles reveal that sediment waves consistently migrate up-slope through time (Fig. 10). Sediment cores from segments with sediment waves (PV9-G1 and DR136 VC-134) constrain the bedforms as fine-grained, comprised of dominantly silt with minor clay and very fine to fine-grained sand turbidites (Table 1; Fig. 13), as found elsewhere (e.g., Wynn and Stow, 2002; Kostic, 2011). Although there are not enough subsurface data to definitively distinguish between antidune (Normark et al., 1980) or cyclic step (Fildani et al., 2006; Kostic and Parker, 2006) origin of the Palos Verdes slope sediment waves, the cross-sectional symmetry, up-slope migration (Fig. 10), fine-grained sediment (Fig. 13), short wavelengths (Fig. 7), and gradients (Table 2; Fig. 5) suggest that the sediment waves may be antidunes or transitional bedforms (e.g., Normark et

al., 1980; Cartigny et al., 2011, 2014; Kostic, 2011, 2014), such that basic calculations of flow height and concentration can be reasonably estimated.

Using the simplified antidune model from Normark et al. (1980), sediment concentration and flow height can be estimated for each segment using average wavelength. Flow velocity (U) is estimated as 10 cm/s for the deposition of silt-sized sediment (Normark et al., 1980) and for flows originating from failed slope deposits (e.g., Talling et al., 2013). Dimensionless flow concentration C is calculated with the equation (Normark et al., 1980; Wynn et al., 2000b):

$$C \cong \frac{2\pi}{1.6g} \times \frac{U^2}{L} \cong 0.0004 \times \frac{U^2}{L}$$

For this basic estimated calculation, g is the acceleration of gravity (980 cm/s^2) and L is the average wavelength in centimeters for each segment. Estimated sediment concentrations are 4.8*10^{-5}, 6.2*10^{-5}, 3.7*10^{-5}, and 5.9*10^{-5} for segments (2) through (5), respectively (Table 2). Likewise, flow height is estimated from wavelength for flows with Froude numbers close to 1 (Normark et al., 1980; Wynn et al., 2000b):

$$h \cong \frac{L}{2\pi}$$

where L is again the average wavelength from each segment and h is the flow height in the same dimensions as the wavelength. Estimated flow heights are ~1/6 the wavelength, resulting in ~13 m, ~10 m, ~17 m, and ~10 m flow heights for segments (2) through (5), respectively (Table 2). These values suggest that the flows expand (increase in flow height) and deposit (decrease in concentration) as they transition to shallower gradients (Table 2, Fig. 6).

5.3. Gradient influence on deposition

Observed correlations between gradient, seafloor morphology, Holocene sediment thickness, grain size, and flow deposits provide constraints for deep-marine sediment flow morphodynamics. Restraining and releasing bends and minor step-overs in the active Palos Verdes Fault create and maintain breaks in gradient that separate different sedimentary process domains, characterized by variations in seafloor morphology and deposit geometry. The channel and adjacent overbank areas in segment (1) appear to have been dominantly a region of bypass (e.g., Hubbard et al., 2014; Stevenson et al., 2015), particularly in the channel thalweg, where bypass and (or) erosion created a thinner Holocene section from flows that continued down slope to preferentially deposit in areas of decreased gradient (e.g., Fig. 13). The segment (2) depocenter appears to be a dynamic area of deposition, erosion, and bypass, where sand-rich basal portions of sediment gravity flows were deposited at the break in gradient, and finer portions of the stratified flows continued to depocenters down slope (e.g., Fig. 13). After segments (1) through (3), any remaining sand and some mud-rich portions of the flows were deposited at the break in gradient associated with the segment (4) pull-apart basin. This basin appears to contain the most complete record of Holocene flows along this continental slope depositional system (Fig. 13).

The finest fractions of the flows appear to have bypassed the basin and continued down slope to the segment (7) depocenter (Fig. 13), although clay flocculation may have resulted in effective grain sizes approaching those in up-slope depocenters. The submarine landslide that created the upper headwall occurred prior to the Holocene at ~31 ka (Brothers et al., 2015), so breaks in gradient at the upper headwall would have existed during accumulation of the Holocene sediment package, resulting in consistent bypass along the upper headwall and deposition in segment (7). Thickness of Holocene sediments in the segment (7) depocenter, little indication of erosion, and prevalence of the finest-grained

portion of the flow deposits all suggest that this was a terminal deposit for Holocene flows along this section of the continental slope.

Interactions between fault-controlled seabed gradient and passing sediment flows explain depositional patterns and stratigraphic architecture. Tectonic control is a common interpretation in other settings with active tectonics, but most examples involve channels that trend down-slope nearly perpendicular to faulting (e.g., Nelson and Maldonado, 1988; Cronin, 1995; Adeogba et al., 2005; Le Dantec et al., 2010; Perez-Hernandez et al., 2014). In this study, the channel parallels an active fault strand, making the same minor bend just below ~350 m water depth (Fig. 4). However, the resulting gradient rather than the faulting appears to be a greater influence on deposition and morphology. Although faults trend roughly down-slope in the study area, minor bends and step-overs create transpressional and transtensional segments that result in down-slope gradient and architecture variations similar to slope-perpendicular faulting and other channels that cross down-slope segments with varying gradient (e.g., Adeogba et al., 2005; Maier et al., 2013). Flows emanating from the channel appear to have spanned the active fault strands without being diverted. For example, the western margin of the low-relief channel is created by the Palos Verdes Fault, but the channel is not fault-controlled because it loses confinement at a break in gradient, causing a morphodynamic transition from segment (1) channel to segment (2) depocenter. The channel appears to be a higher-order architectural unit, feeding numerous deposits into the wider and deeper depocenters that expand down slope (e.g., Fig. 13).

The influence of gradient documented in this study confirms the importance of gradient widely interpreted in modern and ancient systems (Stow et al., 1983; Normark and Piper, 1991; Haughton, 2000; Kneller, 2003; Adeogba et al., 2005; Ferry et al., 2005; McHargue et al., 2011 and many others). In this study, continued Holocene fault motion and

maintenance of gradient prohibits an equilibrium profile (e.g., Ross et al., 1994; Pirmez et al., 2000; Kneller, 2003; Samuel et al., 2003; Ferry et al. 2005) from being reached. Instead, the fault creates consistent segments for deposition and bypass through time, such that deposition towards an equilibrium profile is reflected in the Holocene isopach that can be related to seafloor gradient (Figs. 5–6).

Abrupt decreases in gradient are increasingly recognized as important to deep-sea flow processes, sediment transport, and depositional architecture (e.g., Piper et al., 1999; Fildani et al., 2006, 2013; Piper and Normark, 2009) through the generation of hydraulic jumps that lead to scouring or bypass followed by enhanced deposition of sediment entrained in the flow (Komar, 1971; García, 1993). Such hydraulic jumps and deposition appear to have occurred with minimal erosion in the study area, where breaks in gradient of ~1.5° result in depocenters of segments (2) and (4) with Holocene sediment thickness increases >3 m (Table 2; Figs. 5–6). Slightly back-sloped gradient at segment (6) may be related to erosion at the hydraulic jump adjacent to the upper headwall. Smaller increases in Holocene sediment accumulation of less than 1 m within segments (3) and (5) correspond to gradient decreases of ~0.5° (Figs. 5–6) and may also represent the effects of hydraulic jumps. Estimated flow concentrations decrease and estimated flow heights increase at the break in gradient of ~1.5° at the transition into the segment (4) pull-apart basin depocenter (Table 2), owing to enhanced deposition and expansion at the change in gradient and possibly a hydraulic jump. The same break in gradient results in a ~0.1 m decrease in sediment wave height and an ~40 m increase in sediment wavelength (Table 2; Figs. 7). Similar correlations of sediment wave dimensions and seafloor gradient are established in other settings, but for orders of magnitude larger sediment waves (e.g., Migeon et al., 2000; Wynn et al., 2000a,b; Ercilla et al., 2002a,b; Normark et al., 2002).

The Palos Verdes slope high-resolution dataset provides a unique opportunity to measure and document sediment gravity flow morphodynamic response to gradient. Three main factors in combination allow this quantification: 1) The active Palos Verdes Fault. Gradient is maintained through the Holocene by the Palos Verdes Fault such that deposition and erosion do not result in a significant alteration of seafloor gradient through time. 2) Holocene sedimentation. Holocene sediment gravity flows and related sediment accumulation on the Palos Verdes slope recorded depositional and tectonic processes. 3) High-resolution geophysical imaging and targeted sampling. The high resolution of the dataset allows the correlation of cores with seismic reflections and sub-meter-scale changes in seafloor morphology related to gradient shifts of only 0.5°.

Quantitative results presented here constrain the morphodynamic sensitivity of sediment gravity flows to gradient and may aid future numerical modeling studies of flow processes in both active and passive margin settings. Context provided by grids of AUV data and targeted samples suggest that deposits change with only minor shifts in gradient. Results of this study allow identification of depocenters such that condensed sections or most-complete records of flow deposits could be targeted for additional sampling or further analysis. This detailed understanding of depositional architecture is particularly important in studies of submarine paleoseismology targeting secondary evidence of earthquakes, where slight variations in turbidite records have large implications for hazard assessment (e.g., Goldfinger et al., 2003, 2007; Atwater et al., 2014).

6. Conclusions

Restraining and releasing bends and minor step-overs of the active Palos Verdes Fault created and maintained breaks in gradient that separate segments of the slope with

differing Holocene sediment accumulation, grain size of flow deposits, and morphology. Holocene deposition of fine-grained sediments (average silt size) is inversely correlated to small changes in underlying gradient of ~0.5° or more. Depocenters occur where breaks in gradient of ~1.5° cause down-slope flows to deposit up to 4 m of Holocene sediment. Sediment waves (λ = ~100 m, h=<2 m) are an order of magnitude smaller than most other published examples but display similar correlation with gradient. Decreased gradient of ~1.5° into a fault-controlled pull-apart depocenter causes a decrease in average sediment wave height of ~0.1 m and a >40 m increase in wavelength. Small-scale bedforms imaged in this study, such as sediment waves, are likely more abundant than recognized from existing regional maps. Our results may provide important constraints for future modeling of sediment flow dynamics across active and passive margin settings.

ACKNOWLEDGEMENTS

This research was funded by the U.S. Geological Survey (USGS) Pacific Coastal and Marine Science Center (PCMSC) Coastal and Marine Earthquake, Tsunami and Landslide Active Margin Field Studies Project and by the Monterey Bay Aquarium Research Institute (MBARI) through the David and Lucile Packard Foundation. We are grateful for assistance from Angela Tan, Elliot Taewook Kim, Pete Dartnell, Rendy Keaten, Eve Lundsten, Krystle Anderson, Mike Torresan, Ray Sliter, Hans Thomas, Anthony Kovscek, the MBARI ROV pilots, the MBARI AUV team, the science parties and crews of the *R/V Zephyr*, *R/V Western Flyer*, and *R/V Sproul*, and PCMSC core and sediment laboratories. We thank Neil Mitchell, Andrea Fildani, and Nancy Prouty for providing helpful reviews. This research builds on previous work in the southern California Borderland by Bill Normark, Brian Edwards, Holly Ryan, and many others without whom this study would not be possible.

REFERENCES

Adeogba, A.A., McHargue, T.R., Graham, S.A., 2005. Transient fan architecture and depositional controls from near-surface 3-D seismic data, Niger Delta continental slope. AAPG Bull. 89, 627–643.

Atwater, B.F., Carson, B., Griggs, G.B., Johnson, H.P., Salmi, M.S., 2014. Rethinking turbidite paleoseismology along the Cascadia subduction zone. Geology 42, 827–830.

Bernhardt, A., Melnick, D., Jara-Munõz, J., Argandoña, B., González, J., Strecker, M., 2015. Controls on submarine canyon activity during sea-level highstands: The Biobío canyon system offshore Chile. Geosphere 11, 1226–1255.

Bohannon, R.G., Geist, E., 1998. Upper crustal structure and Neogene tectonic development of the California continental borderland. Geol. Soc. Am. Bull. 110, 779–800.

Bouma, A.H., 1962. Sedimentology of some flysch deposits. Elsevier, New York, 168 pp.

Brothers, D.S., Conrad, J.E., Maier, K.L., Paull, C.K., McGann, M., Caress, D.W., 2015. The Palos Verdes Fault offshore southern California: Late Pleistocene to Present tectonic geomorphology, seascape evolution and slip-rate estimate based on AUV and ROV surveys. J. Geophys. Res. Solid Earth 120, 4734–4758.

Brothers, D.S., ten Brink, U.S., Andrews, B.D., Chaytor, J.D., 2013. Geomorphic characterization of the U.S. Atlantic continental margin. Mar. Geol. 338, 46–63.

Caress, D.W., Chayes, D.N., 1996. Improved processing of Hydrosweep DS Multibeam Data on the *R/V Maurice Ewing*. Mar. Geophys. Res. 18, 631–650.

Caress, D.W., Thomas, H., Kirkwood, W.J., McEwen, R., Henthorn, R., Clague, D.A., Paull, C.K., Paduan, J., Maier, K.L., 2008. High-resolution multibeam, sidescan, and subbottom surveys using the MBARI AUV D.

Allan B, in: Reynolds, J.R., Greene, H.G. (Eds.), Marine Habitat Mapping Technology for Alaska Alaska Sea Grant College Program, University of Alaska Sea Grant College Program, University of Alaska Fairbanks, doi: 10.4027/mhmta.2008.04.

Cartigny, M.J.B., Postma, G., van den Berg, J.H., Mastbergen, D.R., 2011. A comparative study of sediment waves and cyclic steps based on geometries, internal structures and numerical modeling. Mar. Geol. 280, 40–56.

Cartigny, M.J.B., Ventra, D., Postma, G., van den Berg, J.H., 2014. Morphodynamics and sedimentary structures of bedforms under supercritical-flow conditions: New insights from flume experiments. Sedimentology 61, 712–748.

Covault, J.A., Fildani, A., 2014. Continental shelves as sediment capacitors or conveyors: Source-to-sink insights from the tectonically active Oceanside shelf, southern California, USA. Geolog. Soc. Am. Mem. 41, 315–326.

Covault, J.A., Romans, B.W., 2009. Growth patterns of deep-sea fans revisited: Turbidite-system morphology in confined basins, examples from the California Borderland. Mar. Geol. 265, 51–66.

Covault, J.A., Normark, W.R., Romans, B.W., Graham, S.A., 2007. Highstand fans in the California borderland: The overlooked deep-water depositional systems. Geology 35, 783–786.

Covault, J.A., Kostic, S., Paull, C.K., Ryan, H.F., Fildani, A., 2014. Submarine channel initiation, filling and maintenance from sea-floor geomorphology and morphodynamic modeling of cyclic steps. Sedimentology 61, 1031–1054.

Cronin, B.T., 1995. Structurally-controlled deep-sea channel courses: examples from the Miocene of southeast Spain and the Alboran Sea, southwest Mediterranean, in: Hartley, A.J., Prosser, D.J., (Eds.), Characterization of Deep Marine Clastic Systems, Geol. Soc. Am. Spec. Publ. 94, 115–135.

Crouch, J.K., 1981. Northwest margin of California Continental Borderland: Marine Geology and Tectonic Evolution. AAPG Bull. 65, 191–218

Crouch, J.K., Suppe, J., 1993. Late Cenozoic tectonic evolution of the Los Angeles basin and inner California borderland: A model for core complex-like crustal extension. Geol. Soc. Am. Bull. 105, 1415–1434.

Dartnell, P., Gardner, J.V., 1999. Seafloor images and data from multibeam surveys in San Francisco Bay, southern Caliofrnia, Hawaii, the Gulf of Mexico, and Lake Tahoe, California-Nevada. U.S. Geol. Surv. Digital Data Series DDS-55, version 1 (CD-ROM).

Dartnell, P., Conrad, J.E., Ryan, H.F., Finlayson, D.P., 2014. Bathymetry and acoustic backscatter—outer mainland shelf and slope, Gulf of Santa Catalina, Southern California. U.S. Geol. Surv. Open-File Report 2014-1094.

Dartnell, P., Driscoll, N.W., Brothers, D.S., Conrad, J.E., Kluesner, J., Kent, G., Andrews, B.D., 2015. Colored shaded-relief bathymetry, acoustic backscatter, and selected perspective views of the Inner Continental Borderland, southern California. U.S. Geol. Surv. Scientific Investigations Map 3324.

Dolan, J.F., Bowman, D.D., Sammis, C.G., 2007. Long-range and long-term fault interactions in Southern California. Geology 35, 855–858.

Ercilla, G., Alonso, B., Wynn, R.B., Baraza, J., 2002a. Turbidity current sediment waves on irregular slopes: observations from the Orinoco sediment-wave field. Mar. Geol. 192, 171–187.

Ercilla, G., Wynn, R.B., Alonso, B., Baraza, J., 2002b. Initiation and evolution of turbidity current sediment waves in the Magdalena turbidite system. Mar. Geol. 192, 153–169.

Ferry, J.-N., Mulder, T., Parize, O., Raillard, S., 2005. Concept of equilibrium profile in deep-water turbidite systems: effects of local physiographic changes on the nature of sedimentary processes and the geometries of deposits, in: Hodgson, D.M., Flint, S.S. (Eds.), Submarine Slope Systems: Processes and Products, Geol Soc. London, Spec. Publ. 244, 181–193.

Fildani, A., Normark, W.R., Kostic, S., Parker, G., 2006. Channel formation by flow stripping: large-scale scour features along the Monterey East Channel and their relation to sediment waves. Sedimentology 53, 1265–1287.

Fildani, A., Hubbard, S.M., Covault, J.A., Maier, K.L., Romans, B.W., Traer, M., Rowland, J., 2013. Erosion at inception of deep-sea channels. Mar. Petrol. Geol. 41, 48–61.

Fisher, M.A., Langenheim, V.E., Nicholson, C., Ryan, H.F., Sliter, R.W., 2009. Recent developments in understanding the tectonic evolution of the Southern California offshore area: Implications for earthquake-hazard analysis. Geol. Soc. Amer. Spec. Pap. 454, 229–250.

Fleming, K., Johnston, P. Zwartz, D., Yokoyama, Y., Lambeck, K., Chappell, J., 1998. Refining the eustatic sea-level curve since the Last Glacial Maximum using far- and intermediate-field sites. Earth Plant. Sci. Lett. 163, 327–342.

García, M.H., 1993. Hydraulic jumps in sediment-driven bottom currents. J. Hydraul. Eng. 119, 1094–1117.

Gardner, J.V., Dartnell, P., 2002. Multibeam mapping of the Los Angeles, California margin: U.S. Geol. Surv. Open-File Report 2002-162.

Geogiopoulou, A., Cartwright, J.A., 2013. A critical test of the concept of submarine equilibrium profile. Mar. Petrol. Geol. 41, 35–47.

Goldfinger, C., Nelson, C.H., Johnson, J.E., the Shipboard Scientific Party, 2003. Deep-water turbidites as Holocene earthquake proxies: the Cascadia subduction zone and Northern San Andreas Fault systems. Ann. Geophys. 46, 1169–1194.

Goldfinger, C., Morey, A.E., Nelson, C.H., Gutiérrez-Pastor, J., Johnson, J.E., Karabanov, E., Chaytor, J., Eriksson, A., Shipboard Scientific Party, 2007. Rupture lengths and temporal history of significant earthquakes on the offshore and north coast segments of the Northern San Andreas Fault based on turbidite stratigraphy. Earth Planet. Sci. Lett. 254, 9–27.

Gong, C., Wang, Y., Peng, X., Li, W., Qiu, Y., Xu, S., 2012. Sediment waves on the South China Sea Slope off southwestern Taiwan: Implications for the intrusion of the Northern Pacific Deep Water into the South China Sea. Mar. Petrol. Geol. 32, 95–109.

Hampton, M.A., 1972. The role of subaqueous debris flow in generating turbidity currents. J. Sed. Petrol. 42, 775–793.

Haughton, P.D.W., 2000. Evolving turbidite systems on a deforming basin floor, Tabernas, SE Spain. Sedimentology 47, 497–518.

Hodgson, D.M., Flint, S.S., Eds., 2005. Submarine Slope Systems: Processes and Products. Geol Soc. London, Spec. Publ., 244 pp.

Hubbard, S.M., Covault, J.A., Fildani, A., Romans, B.W., 2014. Sediment transfer and deposition in slope channels: deciphering the record of enigmatic deep-sea processes from outcrop. Geolog. Soc. Am. Bull. 126, 857–871.

Ingram, B. L., Southon, J.R., 1996. Reservoir ages in eastern Pacific coastal and estuarine waters. Radiocarbon 38, 573–582.

Klaucke, I., Savoye, B., Cochonat, P., 2000. Patterns and processes of sediment dispersal on the continental slope off Nice, SE France. Mar. Geol. 162, 405–422.

Kneller, B., 2003. The influence of flow parameters on turbidite slope channel architecture. Mar. Petrol. Geol. 20, 901–910.

Komar, P.D., 1971. Hydraulic jumps in turbidity currents. Geol. Soc. Am. Bull. 82, 1477–1488.

Kostic, S., 2011. Modeling of submarine cyclic steps: Controls on their formation, migration, and architecture. Geosphere 7, 294–304.

Kostic, S., 2014. Upper flow regime bedforms on levees and continental slopes: Turbidity current flow dynamics in response to fine-grained sediment waves. Geosphere 10, 1094–1103.

Kostic, S., Parker, G., 2006. The response of turbidity currents to a canyon-fan transition: Internal hydraulic jumps and depositional signatures. J. Hydr. Res. 44, 631–653.

Kuang, Z., Zhong, G., Wang, L., Guo, Y., 2014. Channel-related sediment waves on the eastern slope offshore Dongsha Islands, northern South China Sea. J. Earth Sci. 79, 540–551.

Le Dantec, N., Hogarth, L.J., Driscoll, N.W., Babcock, J.M., Barnhardt, W.A., Schwab, W.C., 2010. Tectonic controls on nearshore sediment accumulation and submarine canyon morphology offshore La Jolla, Southern California. Mar. Geol. 268, 115–128.

Legg, M.R., 1991. Development in understanding the tectonic evolution of the California Continental Borderland, in: Normark, W.R., Piper, D.J.W. (Eds.), Shoreline to Abyss: Contributions in marine geology in honor of Francis P. Shepard, SEPM Sp. Publ. No. 46, 291–312.

Legg, M.R., Goldfinger, C., Kamerling, M.J., Chaytor, J.D., Einstein, D.E., 2007. Morphology, structure and evolution of California Continental Borderland restraining bends. Geol. Soc. Lon. Spec. Publ. 290, 143–168.

Lewis, K.B., Kohn, B.P., 1973. Ashes, turbidites, and rates of sedimentation on the continental slope off Hawkes Bay. New Zealand J. Geol. Geophys. 16, 439–454.

Lowe, D.R., 1982. Sediment gravity flows: II. Depositional models with special reference to the deposits of high-density turbidity currents. J. Sed. Petrol. 52, 279–297.

Maier, K.L., Fildani, A., McHargue, T., Paull, C.K., Graham, S.A., Caress, D.W., 2012. Punctuated deep-water channel migration: High-resolution subsurface data from the Lucia Chica channel system, offshore California. J. Sed. Res. 82, 1–8.

Maier, K.L., Fildani, A., Paull, C.K., Graham, S.A., McHargue, T., Caress, D.W., 2013. Deep-sea channel evolution and stratigraphic architecture from inception to abandonment from high-resolution Autonomous Underwater Vehicle surveys offshore central California. Sedimentology 60, 935–960.

Maier, K.L., Fildani A., Paull, C.K., Graham, S.A., McHargue, T.R., Caress, D.W., McGann, M., 2011. The elusive character of discontinuous deep-water channels: Examples from Lucia Chica, offshore California. Geology 39, 327–330.

Maier, K.L., Paull, C.K., McGann, M., Conrad, J.E., 2016, Sediment core data from offshore Palos Verdes, southern California. U.S. Geol. Surv. data release, http://dx.doi.org/10.5066/FG44NB6.

Marlow, M.S., Gardner, J.V., Normark, W.R., 2000. Using high-resolution multibeam bathymetry to identify seafloor surface rupture along the Palos Verdes fault complex in offshore southern California. Geology 28, 587–590.

McHargue, T., Pyrcz, M.J., Sullivan, M.D., Clark, J.D., Fildani, A., Romans, B.W., Covault, J.A., Levy, M., Posamentier, H.W., Drinkwater, N.J., 2011. Architecture of turbidite channel systems on the continental slope: Patterns and predictions. Mar. Petrol. Geol. 28, 728–743.

Micallef, A., Mountjoy, J.J., Barnes, P.M., Canals, M., Lastras, G., 2014. Geomorphic response of submarine canyons to tectonic activity: Insights from the Cook Strait canyon system, New Zealand. Geosphere 10, 905–929.

Migeon, S., Savoye, B., Faugeres, J.-C., 2000. Quaternary development of migrating sediment waves in the Var deep-sea fan: distribution, growth patter, and implication for levee evolution. Sed. Geol. 133, 265–293.

Mitchell, N.C., Huthnance, J.M., 2008. Oceanographic currents and the convexity of the uppermost continental slope. J. Sed. Res. 78, 29–44.

Mix, A.C., Lund, D.C., Pisias, N.G., Bodén, P., Bornmalm, L., Lyle, M., Pike, J., 1999. Rapid climate oscillations in the northeast Pacific during the last deglaciation reflect Northern and Southern Hemisphere sources, in: Clark, P.U., Webb, R.W., Keigwin, L.D. (Eds.), Mechanisms of global climate change at millennial time scales, Geophysical Monograph 112, 127-148.

Mohrig, D., Marr, J.G., 2003. Constraining the efficiency of turbidity current generation from submarine debris flows and slides using laboratory experiments. Mar. Petrol. Geol. 20, 883–899.

Mutti, E., Normark, W.R., 1987. Comparing examples of modern and ancient turbidite systems: problems and concepts, in: Legget, J.K., Zuffa, G.G. (Eds.) Marine Clastic Sedimentology, Graham & Trotman, London, 1–38.

Nelson, C.H., Maldonado, A., 1988. Factors Controlling Depositional Patterns of Ebro Turbidite Systems, Mediterranean Sea. Am. Assoc. Petrol. Geol. 72, 698–716.

Normark, W.R., Piper, D.J.W., 1983. Navy Fan, California Borderland: Growth pattern and depositional processes. Geo-Mar. Lett. 3, 101–108.

Normark, W.R., Piper, D.J.W., 1991. Initiation processes and flow evolution of turbidity currents: Implications for the depositional record. In: Normark, W.R., Piper, D.J.W. (Eds.) Shoreline to Abyss: Contributions in marine geology in honor of Francis Parker Shepard, SEPM Spec. Publ. No. 46, 207–230.

Normark, W.R., Hess, G.R., Stow, D.A.V., Bowen, A.J., 1980. Sediment waves on the Monterey fan levee: A preliminary physical interpretation. Mar. Geol. 37, 1–18.

Normark, W.R., Piper, D.J.W., Posamentier, H., Pirmez, C., Migeon, S., 2002. Variability in form and growth of sediment waves on turbidite channel levees. Mar. Geol. 192, 23–58.

Normark, W.R., McGann, M., Sliter, R.W., 2009a. Late Quaternary sediment-accumulation rates within the inner basins of the California Continental Borderland in support of geologic hazard evaluation. In: Lee, H.J., Normark, W.R. (Eds.) Earth Science in the Urban Ocean: The Southern California Continental Borderland, Geol. Soc. Am. Spec. Pap. 454, 117–139.

Normark, W.R., Piper, D.J.W., Romans, B.W., Covault, J.A., Dartnell, P., Sliter, R., 2009b. Submarine canyon and fan systems of the California Continental Borderland. In: Lee, H.J., Normark, W.R. (Eds.), Earth Science in the Urban Ocean: The Southern California Continental Borderland, Geol. Soc. Am. Sp. Paper 454, 141–168.

Normark, W.R., Paull, C.K., Caress, D.W., Ussler, W. III, Sliter, R., 2009c. Fine-scale relief related to Late Holocene channel shifting within the floor of the upper Redondo Fan, offshore southern California. Sedimentology 56, 1690–1704.

Nunoura, T., Soffientino, B., Blazejak, A., Kakuta, J., Oida, H., Schippers, A., Takai, K., 2009. Subseafloor microbial communities associated with rapid turbidite deposition in the Gulf of Mexico continental slope (IODP Expedition 308). FEMS Microbiol. Ecol. 69, 410–424.

Paull, C.K., Ussler, W. III, Caress, D.W., Lundsten, E., Covault, J.A., Maier, K.L. Xu, J., Augenstein, S., 2010. Origins of large crescent-shaped bedforms within the axial channel of Monterey Canyon, offshore California. Geosphere 6, 1–20.

Paull, C.K., Caress, D.W., Ussler, W. III, Lundsten, E., Meiner-Johnson, M., 2011. High-resolution bathymetry of the axial channels within Monterey and Soquel submarine canyons, offshore central California. Geosphere 7, 1077–1101.

Paull, C.K., Caress, D.W., Lundsten, E., Gwiazda, R., Anderson, K., McGann, M., Conrad, J., Edwards, B., Sumner, E.J., 2013. Anatomy of the La Jolla Submarine Canyon system; offshore southern California. Mar. Geol. 335, 16–34.

Paull, C.K., McGann, M., Sumner, E.J., Barnes, P.M., Lundsten, E.M., Anderson, K., Gwiazda, R., Edwards, B., Caress, D.W., 2014. Sub-decadal turbidite frequency during the early Holocene: Eel Fan, offshore northern California. Geology 42, 855–858.

Perez-Hernandez, S., Comas, M.C., Escutia, C., 2014. Morphology of turbidite systems within an active continental margin (the Palomares Margin, western Mediterranean). Geomorphology 219, 10–26.

Piper, D.J.W., Normark, W.R., 2009. Processes that initiate turbidity currents and their influence on turbidites: A marine geology perspective. J. Sed. Res. 79, 347–362.

Piper, D.J.W., Cochonat, P., Morrison, M.L., 1999. The sequence of events around the epicenter of the 1929 Grand Banks earthquake: initiation of debris flows and turbidity current inferred from sidescan sonar. Sedimentology 46, 79–97.

Pirmez, C., Beaubouef, R.T., Friedmann, S.J., Mohrig, D.C., 2000. Equilibrium profile and baselevel in submarine channels: examples from Late Pleistocene systems and implications for the architecture of deep-

water reservoir, in: Weimer, P., Slatt, R.M., Coleman, J. (Eds.) Deep-water reservoirs of the world: Gulf Coast Section SEPM Foundation 20th Annual Research Conference, 782–805.

Prins, M.A., Postma, G., Weltje, G.J., 2000. Controls on terrigenous sediment supply to the Arabian Sea during the late Quaternary: the Makran continental slope. Mar Geol. 169, 351–371.

Rona, P.A., 1969. Middle Atlantic continental slope of United States: Deposition and Erosion. AAPG Bull. 53, 1453–1465.

Ross, W.C., Halliwell, B.A., May, J.A., Watts, D.E., Syvitski, J.P.M., 1994. Slope readjustment: A new model for the development of submarine fans and aprons. Geology 22, 511–514.

Ryan, H.F., Legg, M.R., Conrad, J.E., Sliter, R.W., 2009. Recent faulting in the Gulf of Santa Catalina: San Diego to Dana Point, in: Lee, H.J., Normark, W.R. (Eds.), Earth Science in the Urban Ocean: The Southern California Continental Borderland, Geol. Soc. Am. Spec. Pap. 454, 291–315.

Ryan, H.F., Conrad, J.E., Paull, C.K., McGann, M., 2012. Slip rate on the San Diego Trough Fault Zone, Inner California Borderland, and the 1986 Oceanside Earthquake swarm revisited. Bull. Seismol. Soc. Am. 102, 2300–2312.

Samuel, A., Kneller, B., Raslan, S., Sharp, A., Parsons, C., 2003. Prolific deep marine slope channels of the Nile Delta, Egypt. AAPG Bull. 87, 541–560.

Shepard, F.P., 1981. Submarine canyons: Multiple causes and long-time persistence. AAPG Bull. 65, 1061–1077.

Shepard, F.P., Ensele, G., 1962. Sedimentation in the San Diego Trough and contributing submarine canyons. Sedimentology 1, 81–133.

Smith, D.P., Ruiz, G., Kvitek, R., Iampietro, P.J., 2005. Semiannual patterns of erosion and deposition in upper Monterey Canyon from serial multibeam bathymetry. Geol. Soc. Am. Bull. 117, 1123–1133.

Smith, D.P., Kvitek, R., Iampietro, P.J., Wong, K., 2007. Twenty-nine months of geomorphic change in upper Monterey Canyon (2002–2005). Mar. Geol. 236, 79–94.

Sommerfield, C.K., Lee, H.J., Normark, W.R., 2009. Sediment accumulation on the Southern California Bight continental margin during the twentieth century, in: Lee, H.J., Normark, W.R. (Eds.), Earth Science in the Urban Ocean: The Southern California Continental Borderland, Geol. Soc. Am. Spec. Pap. 454, 89–116.

Stevenson, C.J., Jackson, C. A.-L., Hodgson, D.M., Hubbard, S.M., Eggenhuisen, J.T., 2015. Deep-water sediment bypass. J. Sed. Res. 85, 1058–1081.

Stow, D.A.V., Howell, D.G., Nelson, C.H., 1983. Sedimentary, tectonic, and sea-level controls on submarine fan and slope-apron turbidite systems. Geo-Mar. Lett. 3, 57–64.

Stuiver, M., Braziunas, T.F., 1993. Sun, ocean, climate and atmospheric $^{14}CO_2$: an evaluation of causal and spectral relationships. The Holocene 3, 289–305.

Stuiver, M., Polach, H.A., 1977. Discussion: Reporting on ^{14}C date. Radiocarbon 19, 855–858.

Stuiver, M., Reimer, P.J., Reimer, R., 2015. CALIB Radiocarbon Calibration Execute Version 7.0.4, http://calib.qub.ac.uk/calib/

Tubau, X., Paull, C.K., Lastras, G., Caress, D.W., Canals, M., Lundsten, E., Anderson, K., Gwiazda, R., Amblas, D., 2015. Submarine canyons of Santa Monica Bay, Southern California: Variability in morphology and sedimentary processes. Mar. Geol. 365, 61–79.

Traer, M.M., Fildani, A., McHargue, T., Hilley, G.E., 2015. Simulating depth-averaged, one-dimensional turbidity current dynamics using natural topographies. J. Geophys. Res. Earth Surf. 120, 1485–1500.

U.S. Geological Survey and California Geological Survey, 2006. Quaternary fault and fold database for the United States, accessed October 26, 2014, from USGS web site: http://earthquakes.usgs.gov/regional/qfaults.

Vedder, J.G., 1987. Regional geology and petroleum potential of the southern California Borderland, in: Scholl, D.W., Grantz, A., Vedder, J.G. (Eds.), Geology and resource potential of the continental margin of western North America and adjacent ocean basins—Beaufort Sea to Baja California, Circum-Pacific Council for Energy and Mineral Resources 6, 403–447.

Wang, D., Wu, S., Yao, G., Wang, W., 2015. Architecture and evolution of deep-water cyclic deposits in the Qiongdongnan Basin, South China Sea: Relationship with the Pleistocene climate events. Mar. Geol. 370, 43–54.

Warrick, J.A., Farnsworth, K.L., 2009. Sources of sediment to the coastal waters of the Southern California Bight, in: Lee, H.J., Normark, W.R. (Eds.), Earth Science in the Urban Ocean: The Southern California Continental Borderland, Geol. Soc. Am. Spec. Pap. 454, 39–52.

Wynn, R.B., Stow, D.A.V., 2002. Classification and characterisation of deep-water sediment waves. Mar. Geol. 192, 7–22.

Wynn, R.B., Weaver, P.P.E., Ercilla, G., Stow, D.A.V., Masson, D.G., 2000a. Sedimentary processes in the Selvage sediment-wave field, NE Atlantic: new insights into the formation of sediment waves by turbidity currents. Sedimentology 47, 1181–1197.

Wynn, R.B., Masson, D.G., Stow, D.A.V., Weaver, P.P.E., 2000b. Turbidity current sediment waves on the submarine slopes of the western Canary Islands. Mar. Geol. 163, 185–198.

Wynn, R.B., Kenyon, N.H., Masson, D.G., Stow, D.A.V., Weaver, P.P.E., 2002. Characterization and recognition of deep-water channel-lobe transition zones. AAPG Bull. 86, 1441–1462.

Zhong, G., Cartigny, M.J.B., Kuang, Z., Wang, L., 2015. Cyclic steps along the South Taiwan Shoal and West Penghu submarine canyons on the northeastern continental slope of the South China Sea. Geol. Soc. Amer. Bull. 127, 804–824.

TABLES

Table 1 Summary of grain size and depositional environment

Table 2 Summary of averaged parameters by profile segment

FIGURES

Fig. 1. Diagrammatic summary of gradient influence on deposition. (A) An initial seafloor gradient is established at time t_1 where the proximal segment (1) has a much lower gradient (σ_1) than the distal segment (2) (σ_2). Sediment flows that traversed these two segments between t_1 and t_2 resulted in deposition in segment (1) that decreases into segment (2). Higher gradient in segment (2) (σ_2) causes bypass. (B) An initial seafloor gradient is established at time t_1 where the proximal segment (1) has a higher gradient (σ_1) than the distal segment (2) (σ_2). Sediment flows that traversed these two segments between t_1 and t_2 resulted in enhanced deposition on the lower gradient segments.

Fig. 2. Regional setting. Multibeam bathymetric map of offshore southern California Borderland with onshore LANDSAT-8 satellite data (modified from Dartnell et al., 2015), showing the location of this study (boxes indicating Figures 3 and 4 locations). Offshore fault zones are generalized as red lines (modified from U.S. Geological Survey and California Geological Survey, 2006; Ryan et al., 2009; Brothers et al., 2015). NI-RC: Newport-Inglewood-Rose Canyon.

Fig. 3. Study location on the continental slope adjacent to San Gabriel Canyon. Palos Verdes Fault Zone (FZ) traverses the continental shelf and slope. The study area where high-resolution geophysical data were collected with an autonomous underwater vehicle (AUV)

is outlined in white. (A) Color contoured multibeam bathymetry (25 m resolution; 100 m contour interval). AUV tracklines (black) show 150-m-line spacing chirp profile density. (B) Slope map of the region in Part (A).

Fig. 4. Multibeam bathymetry collected with an autonomous underwater vehicle (AUV) (gridded at 2 m; contour interval 50 m). Palos Verdes Fault strands are traced in red and vertical separation is indicated with "u" (upward motion). Closely spaced remotely operated vehicle (ROV) vibracores in the channel transect include (from west to east) DR135 VC-129, DR125 VC-85, DR125 VC-87, DR125 VC-86, DR135 VC-130, DR125 VC-88, DR125 VC-89, DR135 VC-131, and DR125 VC-90. Modified from Brothers et al. (2015).

Fig. 5. Holocene deposition. Location of profiles in Figure 6 are indicated with a dashed black line (from ***A*** to ***B*** to ***C***). (A) Regional shaded relief seafloor map (gridded at 16 m; contour interval 100 m). Potential submarine landslide headwall scarps are highlighted in yellow at the uppermost slope and shelf edge. B) Interpolated Holocene isopach map derived from AUV chirp sub-bottom profiles correlated with radiocarbon ages from sediment cores. See Figure 6 for slope segments (circled numbers). Gravity cores and ROV vibracores are indicated with green and red dots, respectively.

Fig. 6. Correlation of Holocene gradient, sediment thickness, and grain size distributions. (A) Plot of water depth (black) and gradient (blue) in a down-slope profile. See Figure 5A for profile map location. B) Plot of gradient (blue) and interpolated Holocene sediment thickness (red) along a down-slope profile in the AUV survey area. See Figure 5B for profile map location. Segments in the profile (circled numbers) are separated by breaks in

gradient. Projected locations of sediment cores are indicated with dashed vertical black lines. (C) Grain size distributions from sediment core samples are displayed in correlative down-slope units (see Table 1). Vertical gray lines represent averaged D_{50} and D_{90} for each plotted set of flow deposits.

Fig. 7. Seafloor morphology of sediment waves. (A) Slope map of the autonomous underwater vehicle (AUV) multibeam bathymetry. Sediment waves are present from segment (2) through segment (5). (B) Sketch of sediment waves from enlarged portion of Part (A). Numbers represent wavelength (left) and waveheight (right) in meters. Bold numbers are average wavelength to wave height by segment.

Fig. 8. Autonomous underwater vehicle (AUV) chirp sub-bottom profile across the channel and Palos Verdes Fault (PVF) (modified from Brothers et al., 2015). See Figure 4 for profile map location. Core locations are indicated with vertical purple lines. The base Holocene reflection (dashed yellow line) is constrained by radiocarbon ages (see Figures 11–12). Cores were acquired in a transect along this chirp profile, sampling channel thalweg, margin, overbank, and ridge depositional environments.

Fig. 9. Autonomous underwater vehicle (AUV) chirp sub-bottom profile across the pull-apart basin (modified from Brothers et al., 2015). See Figure 4 for profile map location. (A) Holocene deposits progressively thicken into the northeastern side of the basin, suggesting active faulting and deposition during the Holocene. (B) Enlarged portion of profile from Part A. The base Holocene (dashed yellow), mid-Holocene (dashed red), and seafloor reflections are offset at the Palos Verdes Fault, indicating at least three Holocene events (Brothers et al.,

2015). A mid-Holocene reflection (dashed red line) is correlated with an organic-rich flow deposit in cores, including DR136 VC-134.

Fig. 10. Subsurface character of sediment waves. (A) Autonomous underwater vehicle (AUV) chirp sub-bottom profile oriented down slope (modified from Brothers et al., 2015). See Figure 4 for profile map location. Sediment waves are present above the upper headwall in the Holocene sediment package. (B) Enlarged portion of the profile from Part (A), uninterpreted, highlighting the internal structure of the sediment waves. (C) Interpreted profile from Part (B). Blue traced reflections show up-slope migration of the sediment waves. Arrows illustrate changes in trend within one late Pleistocene and Holocene accumulation of sediment waves.

Fig. 11. Remotely operated vehicle (ROV) vibracore correlation panel across the channel transect. See Figure 4 for core locations. Holocene deposits thin onto the transpressional ridge and vary greatly with minor shifts in depositional setting over <220 m across the channel. Cores are displayed as diagrammatic descriptive logs. Radiocarbon ages are shown as calibrated calendar age (cal yr BP) with analytical error next to sampled interval in black. Weight percent sand (white), silt (light gray), and clay (dark gray) from laser particle grain size analyses are represented with pie charts next to sample locations.

Fig. 12. Correlation of flow deposits in vibracore DR125 VC-89 from the channel thalweg with DR135 VC-131 from the channel margin/overbank setting. The slight change in depositional setting over ~32 m lateral distance results in a different depositional record, character, thickness of Holocene sediment, and apparent number of deposits. Cores are

displayed as in Figure 11 with the addition of CT scan images, p-wave velocity (gray), and gamma-ray density (black) logs.

Fig. 13. Correlation panel across a down-slope transect. The Holocene section thickens from the channel thalweg (DR125 VC-89) to the pull-apart basin (DR136 VC-134) and base of the upper headwall (PV2-G1). Variations in depositional setting result in differences in Holocene deposits. Cores are displayed as in Figure 12.

Fig. 14. Grain size distributions derived from laser particle grain size analyses on samples recovered from the channel thalweg (DR125 VC-89) and margin/overbank (DR135 VC-131). Flow deposits are indicated with an asterisk. Sample depths are shown to the right in centimeters.

Fig 15. Grain size distributions derived from laser particle grain size analyses on samples recovered from the mid-Holocene flow deposit across the channel thalweg and eastern channel margin. Each deposit fines upward with a decrease in sand content. The thalweg mid-Holocene flow deposit contains more sand and is thicker than the correlative deposits on the channel margin.

Fig. 16. Grain size distributions derived from laser particle grain size analyses on samples recovered from the down-slope transect. Interpreted flow deposits are indicated with asterisks. Sample depths (in centimeters) are shown to the right.

Table 1
Summary of grain size and depositional environment

Depositional Environment	Segment	Core IDs	*Flow Deposit*								*Background (Hemipelagic, Bioturbated)*							
			Average			*Range*			*Average*		*Average*			*Range*			*Average*	
			% Sand	% Silt	% Clay	# analyses	D50 (μm)	D90 (μm)	Skewness	Kurtosis	% Sand	% Silt	% Clay	# analyses	D50 (μm)	D90 (μm)	Skewness	Kurtosis
Channel Thalweg	(1)	DR125 VC-89	36	53	11	11	15 - 92	54 - 150	1.24	5.3	13	71	16	5	15 - 26	58 - 80	0.69	2.93
Channel Margin (E)	(1)	DR135 VC-131 & DR125 VC-90	31	57	12	7	20 - 83	61 - 141	1.02	4.03	16	70	15	6	19 - 27	65 - 84	0.74	2.98
Channel Margin (W)	(1)	DR125 VC-86 & DR125 VC-87	18	70	12	4	23 - 33	73 - 85	1.04	3.69	-	-	-	0	-	-	-	-
Depocenter	(2)	PV9-G1	51	42	7	4	46 - 87	125 - 136	1.5	5.14	20	66	13	1	30	89	0.96	3.41
Pull-Apart Basin	(4)	DR136 VC-134	24	63	13	14	15 - 70	63 - 157	0.94	3.5	8	75	18	1	30	87	0.76	3.2
Base of Upper Headwall	(7)	PV2-G1	13	70	17	5	12 - 27	53 - 100	0.57	2.78	21	67	12	8	16 - 19	51 - 60	0.61	2.86

Table 2
Summary of averaged parameters by profile segment

Parameter	Segment (1)	Segment (2)	Segment (3)	Segment (4)	Segment (5)	Segment (6)	Segment (7)
depositional environment	*channel*	*depocenter*	*slope*	*pull-apart basin*	*slope*	*upper headwall*	*base of upper headwall*
gradient	1.9°	1.0°	1.2°	0.5°	1.2°	20° - 45°	0°
gradient decrease into depocenters	N/A	1.5°	N/A	1.5°	N/A	N/A	up to 45°
Holocene sediment thickness	2.0 m	3.0 m	1.5 m	3.0 m	1.0 m	0.3 m	4.0 m
max Holocene sediment thickness	2.5 m	4.3 m	2.3 m	4.2 m	1.9 m	0.4 m	4.2 m
wavelength	N/A	83 m	65 m	107 m	68 m	N/A	N/A
wave height	N/A	1.7 m	1.8 m	1.7 m	1.6 m	N/A	N/A
D50 grain size	34 µm	55 µm	N/A	33 µm	N/A	N/A	18 µm
D90 grain size	91 µm	120 µm	N/A	92 µm	N/A	N/A	61 µm
estimated flow height	N/A	~13 m	~10 m	~17 m	~11 m	N/A	N/A
estimated flow concentration	N/A	$4.8 * 10^{-5}$	$6.2 * 10^{-5}$	$3.7 * 10^{-5}$	$5.9 * 10^{-5}$	N/A	N/A

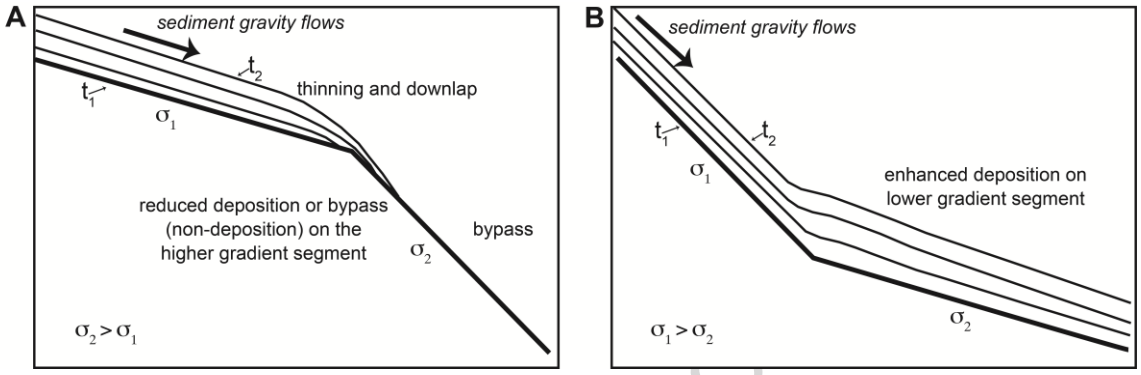

Figure 1

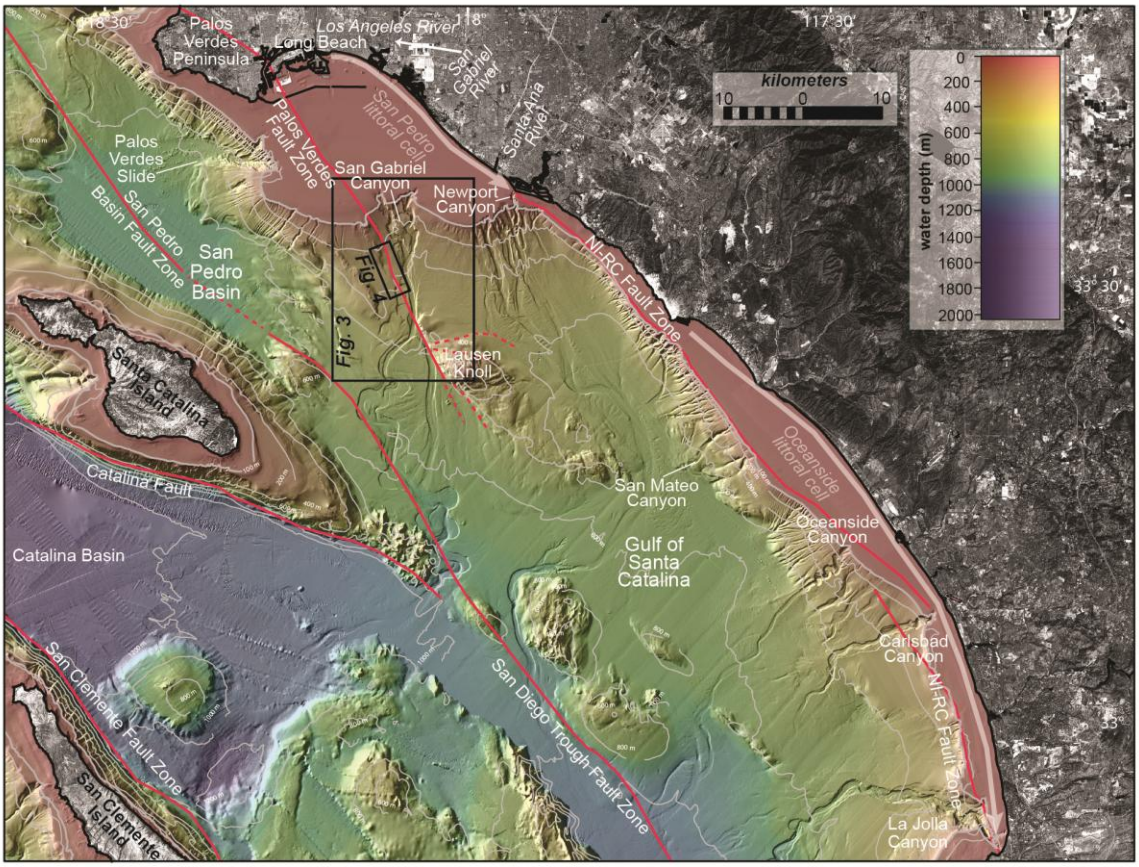

Figure 2

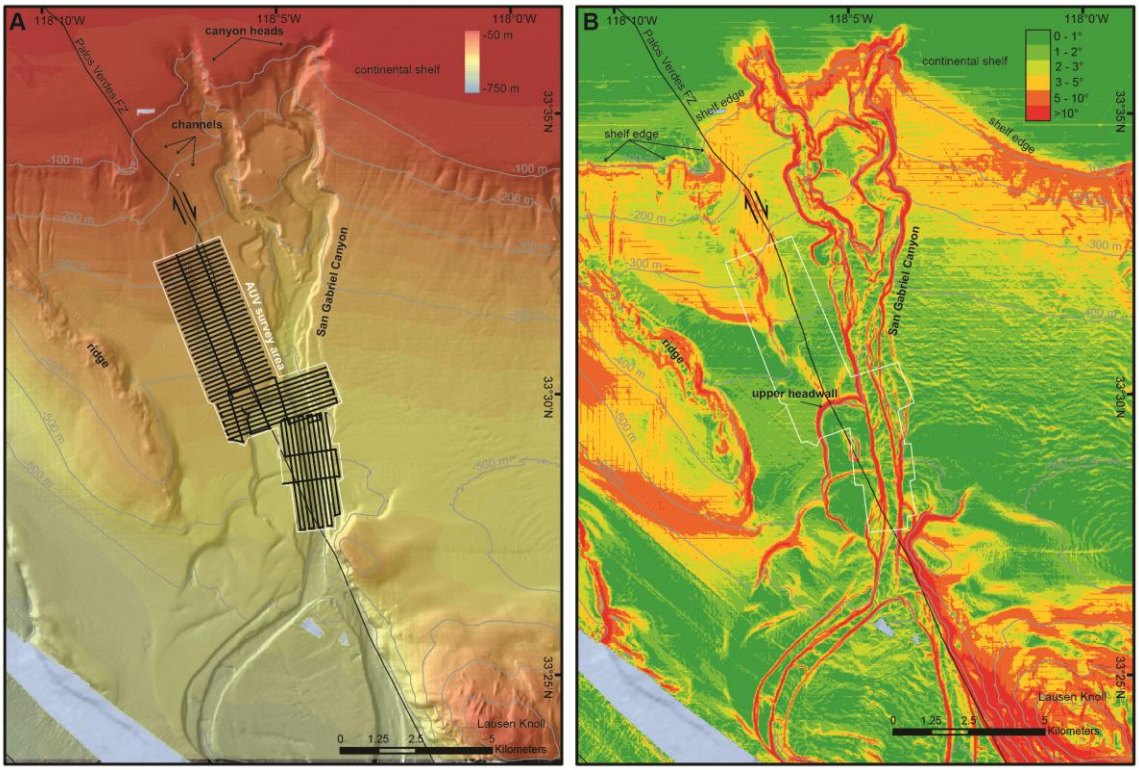

Figure 3

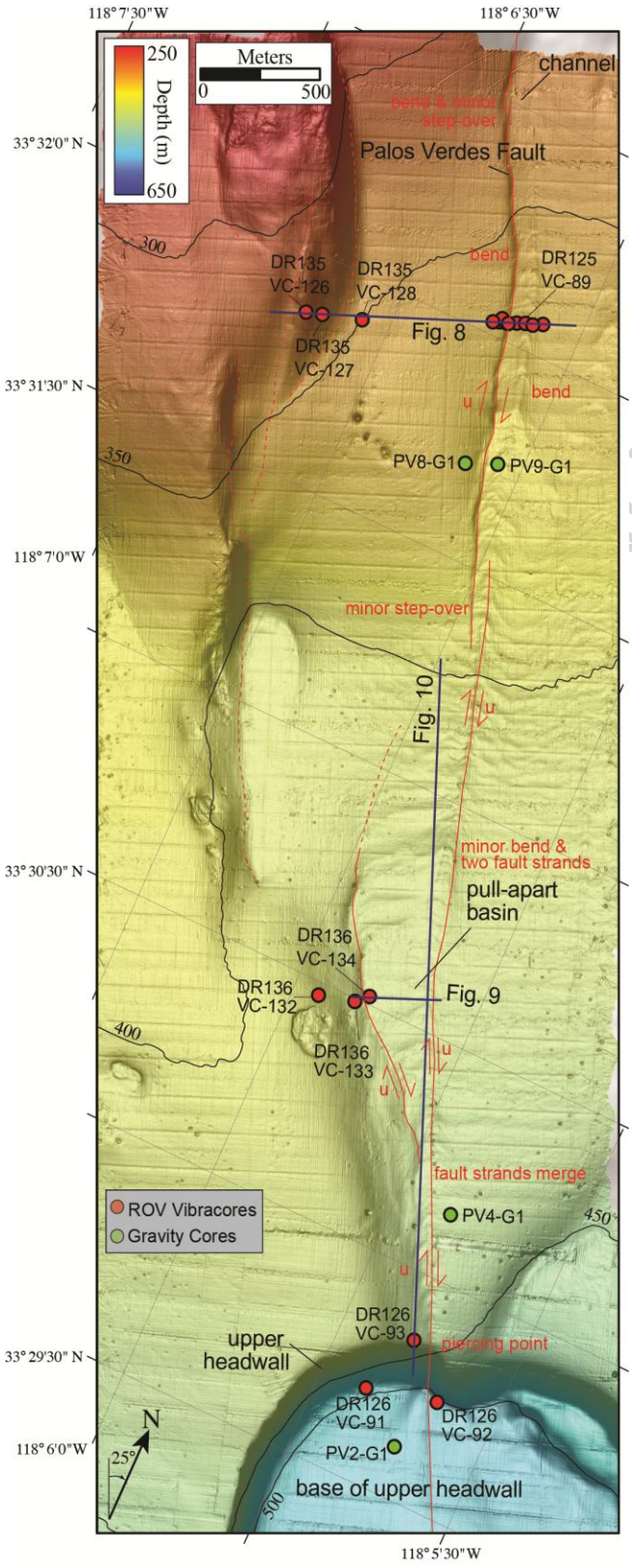

Figure 4

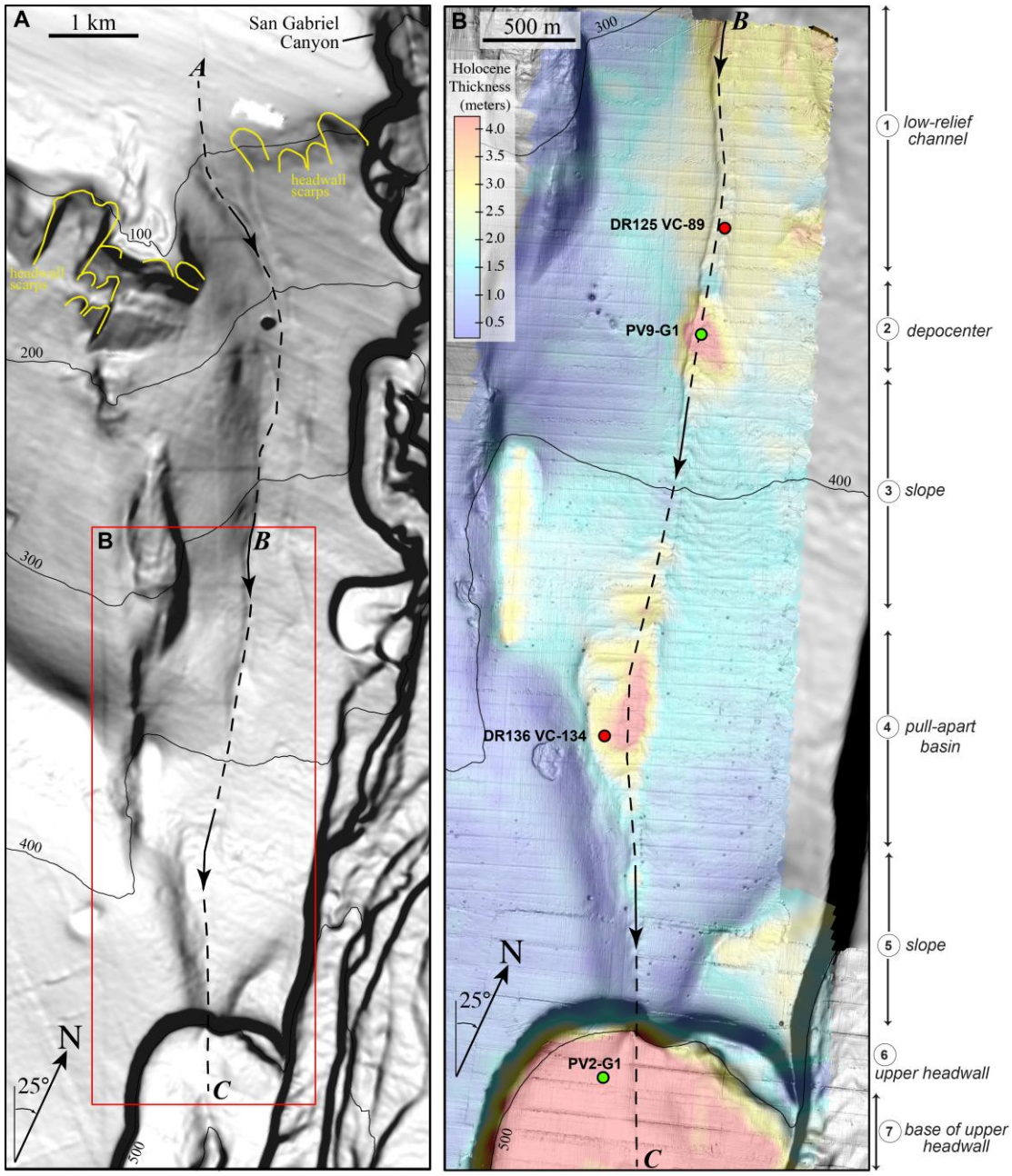

Figure 5

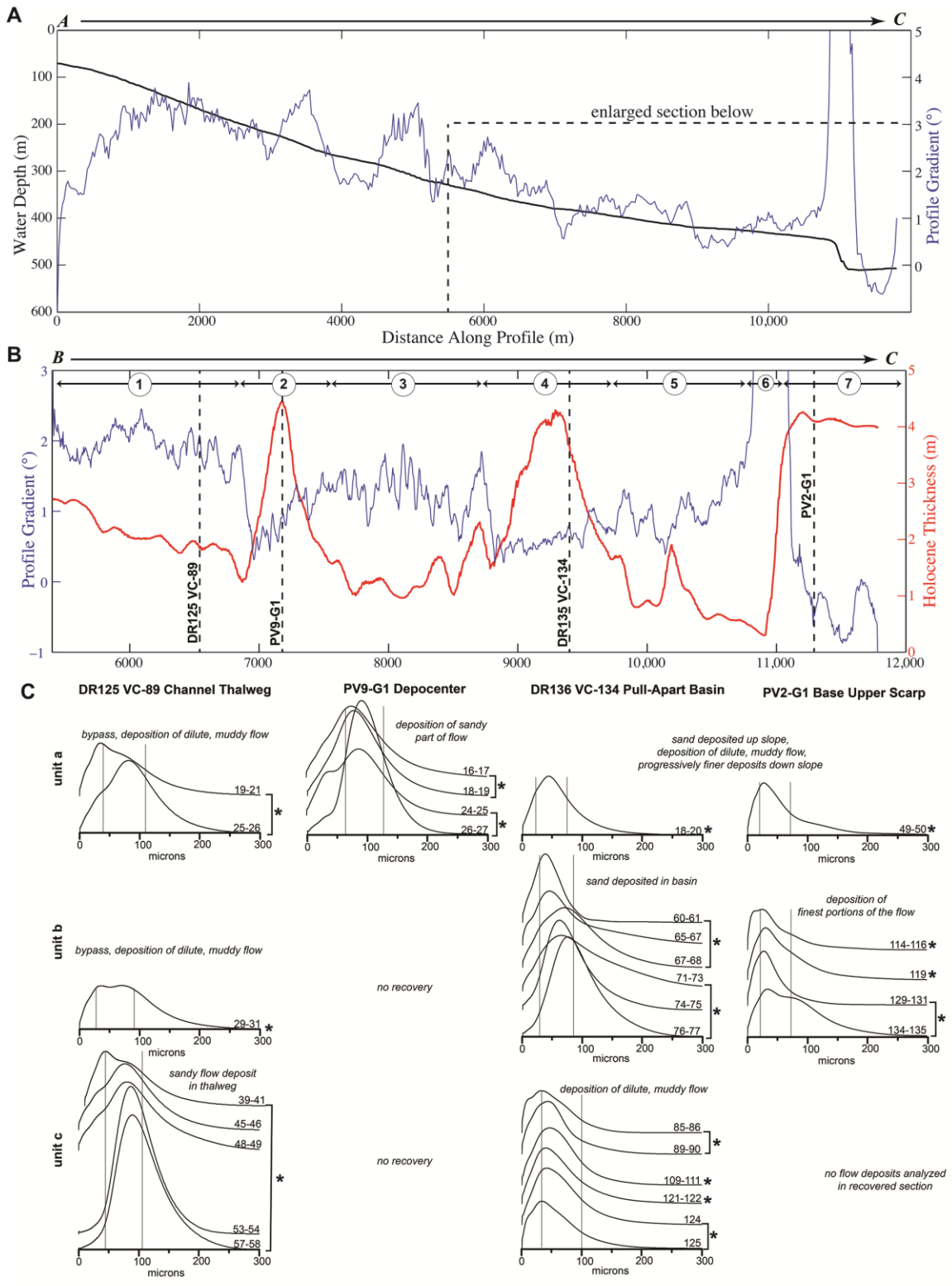

Figure 6

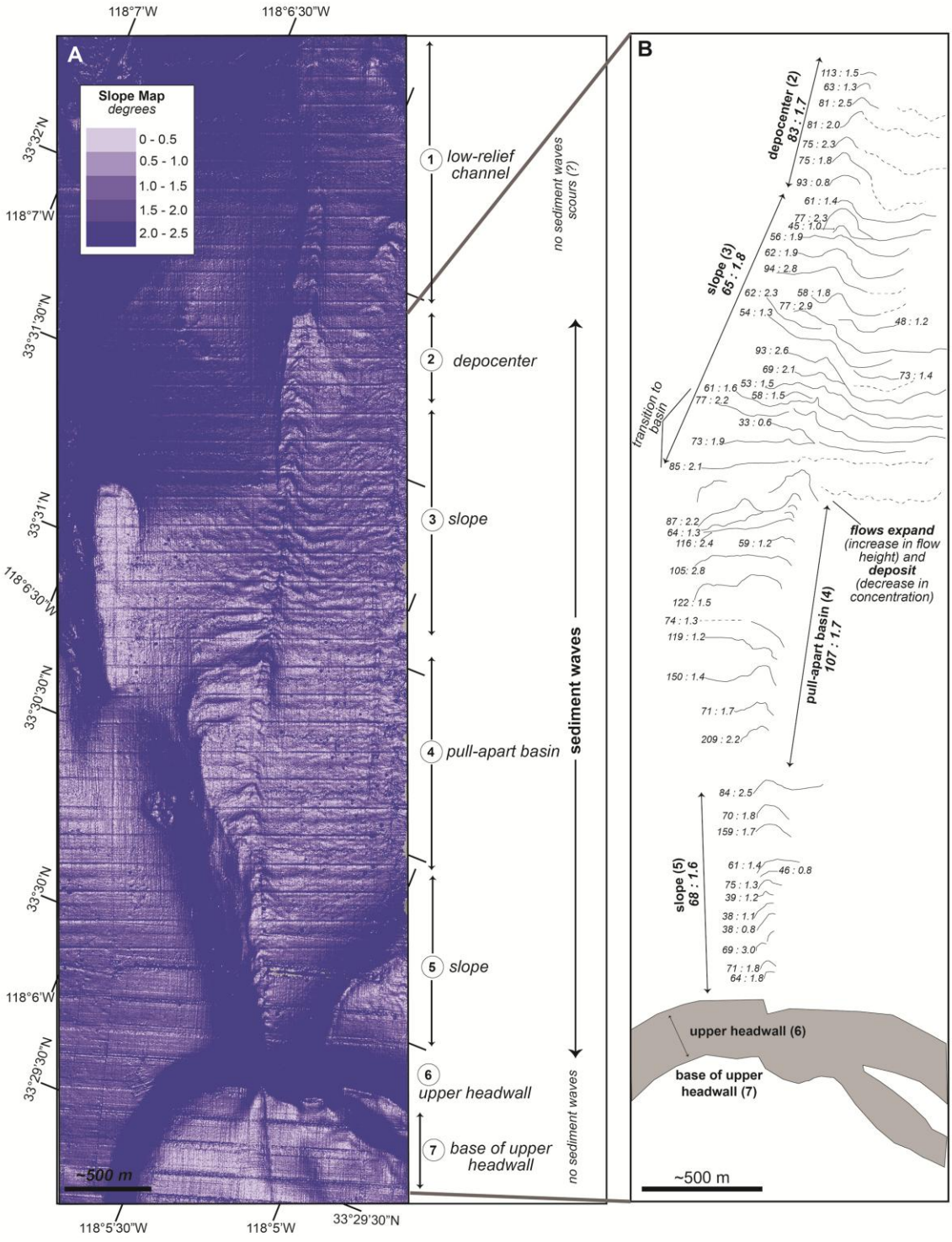

Figure 7

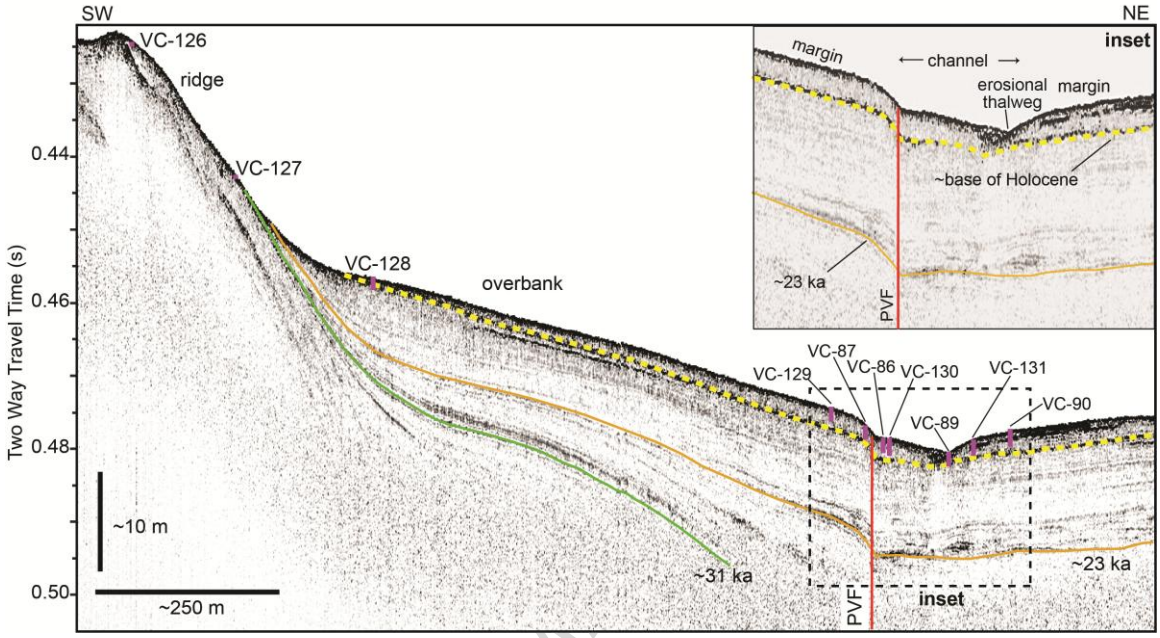

Figure 8

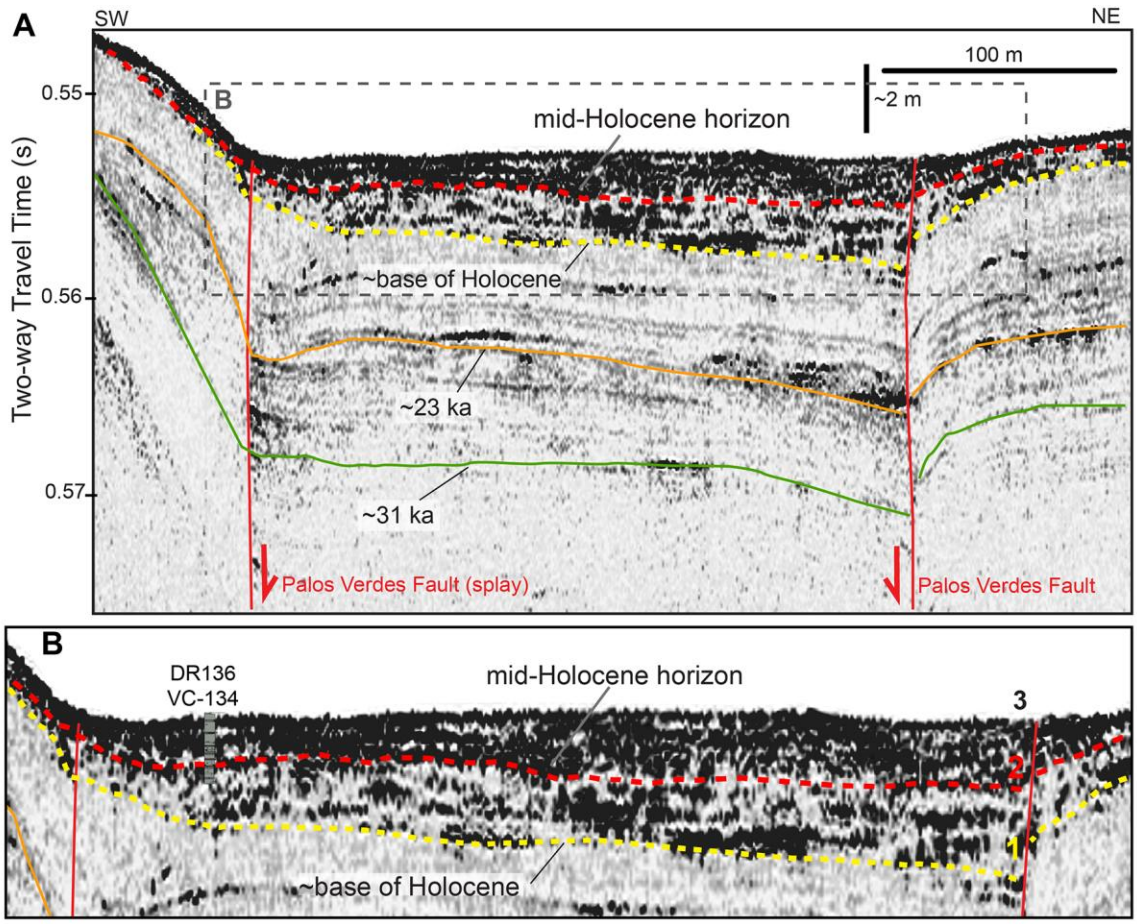

Figure 9

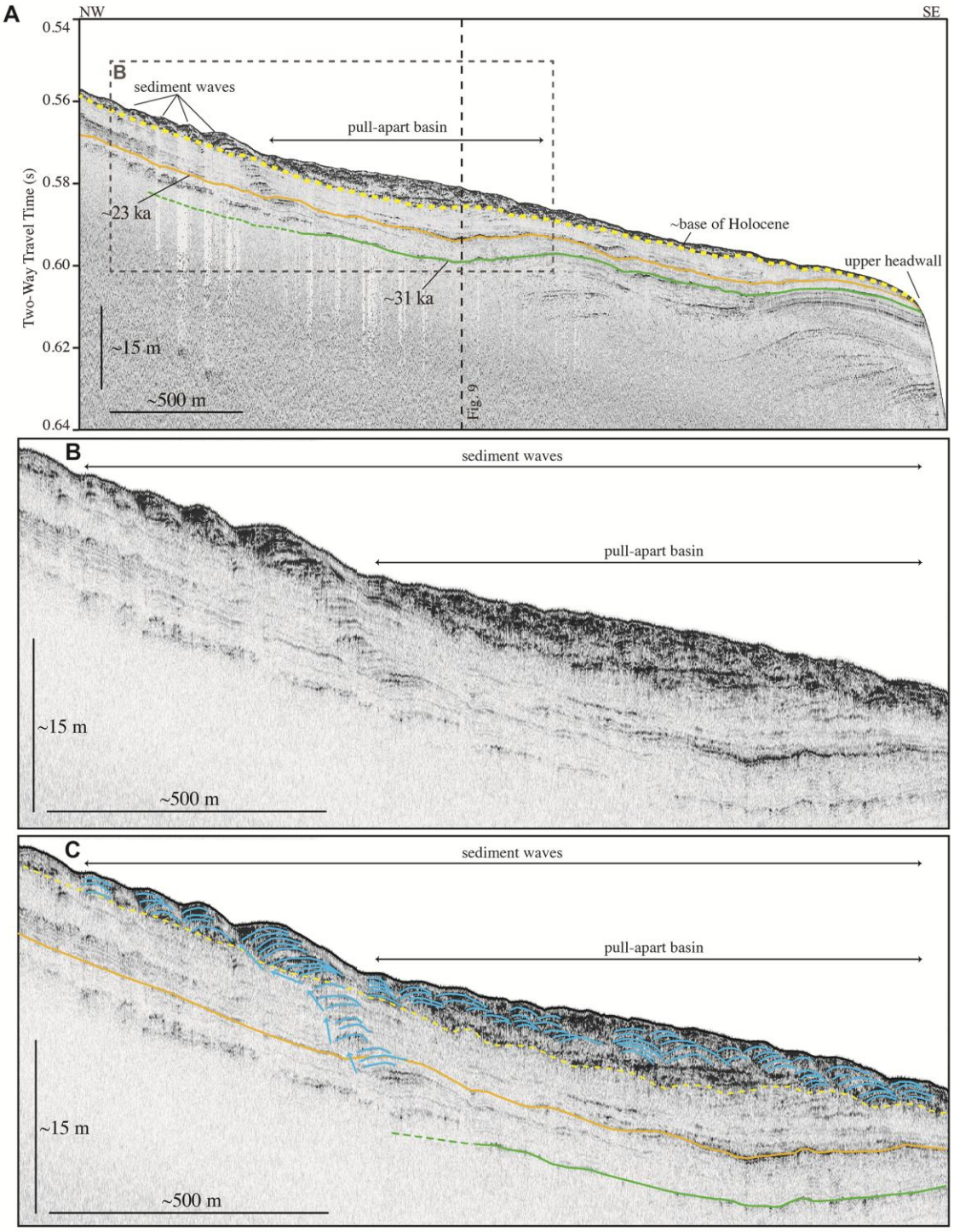

Figure 10

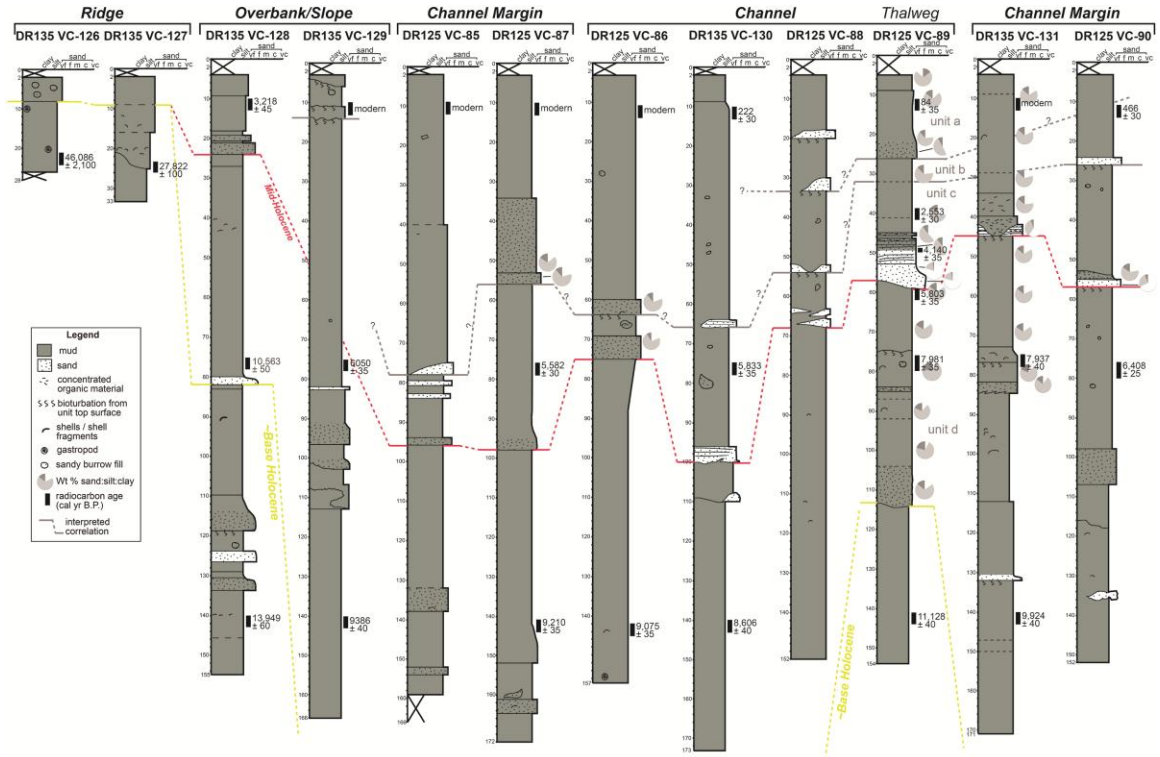

Figure 11

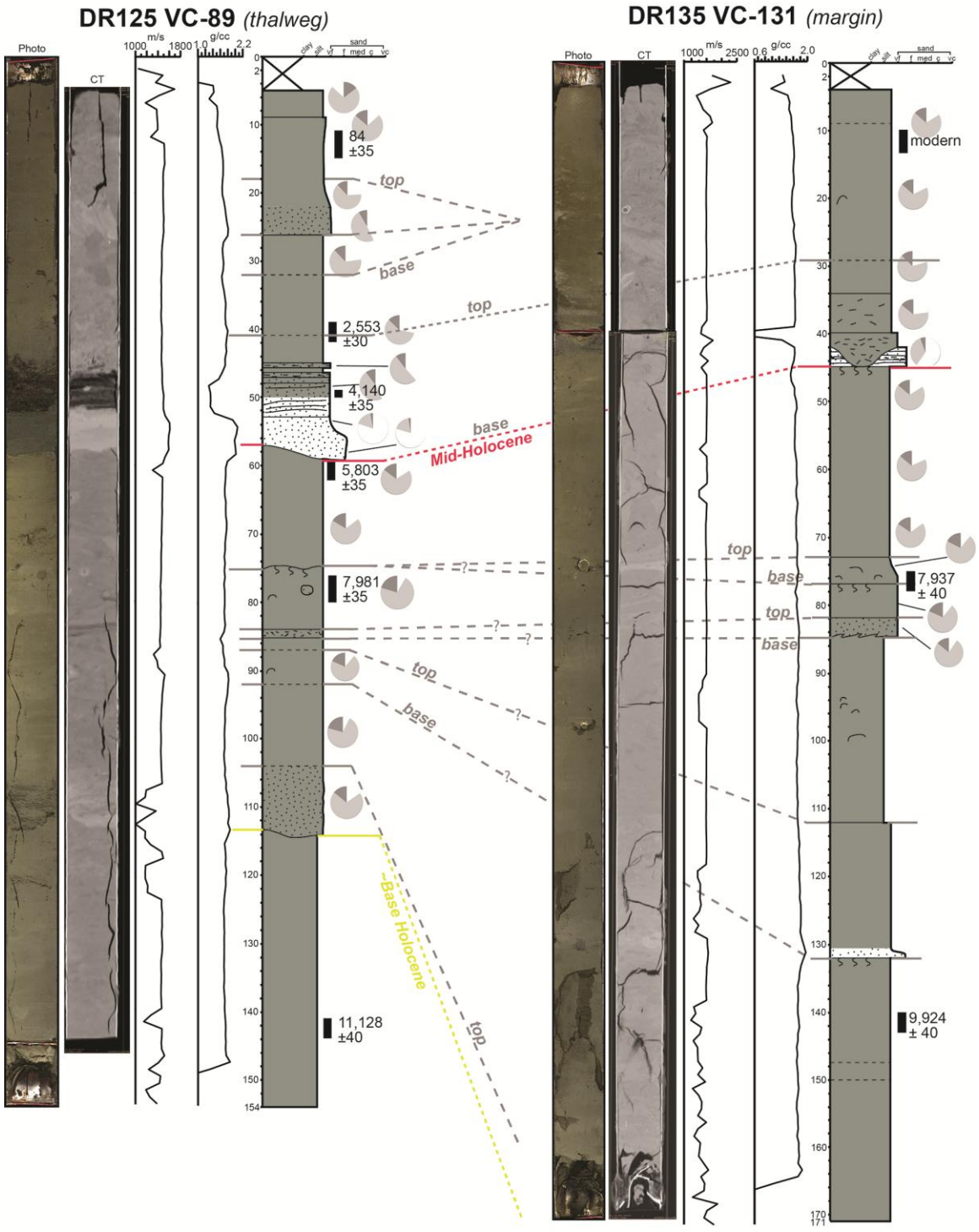

Figure 12

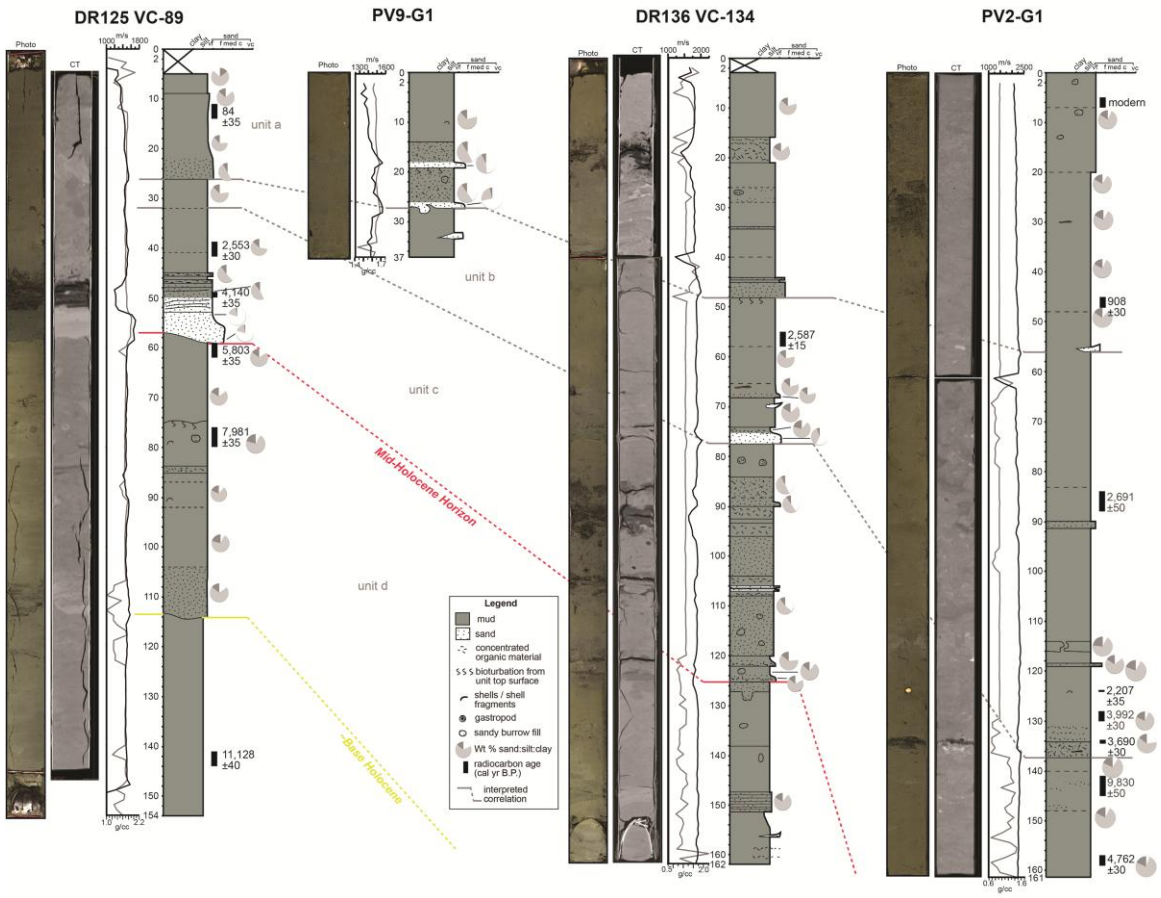

Figure 13

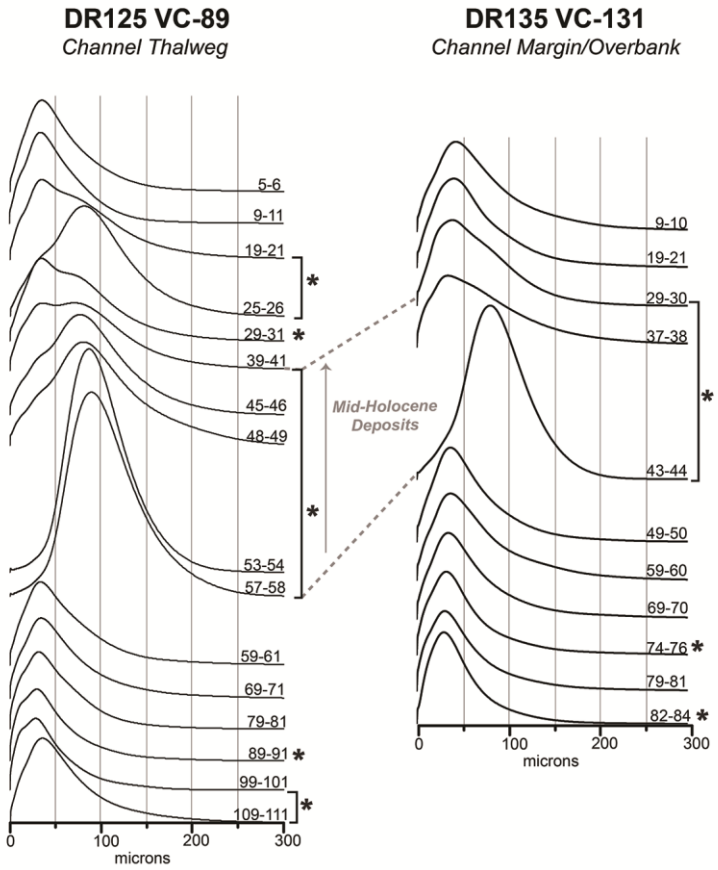

Figure 14

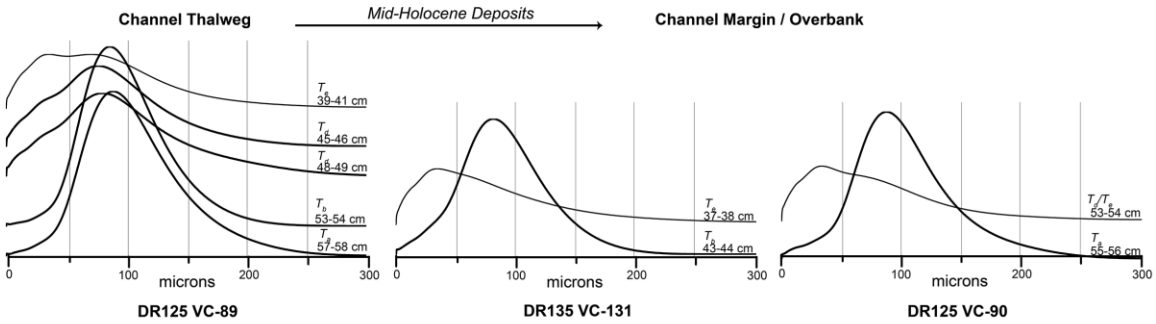

Figure 15

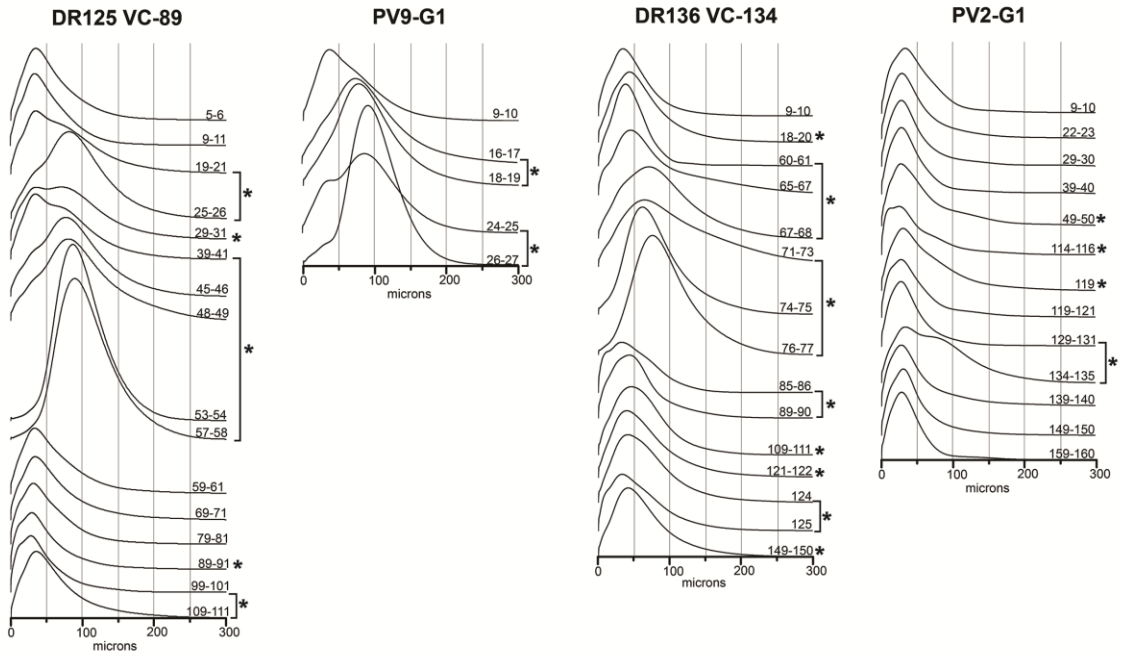

Figure 16

Highlights

- Seabed gradient variations control sediment accumulation and seafloor morphology.

- Active Palos Verdes Fault bends and stepovers maintain gradient breaks.

- Breaks in seabed gradient ≥0.5° trigger increases in sediment accumulation.